The Astronomical Journal, 170:68 (29pp), 2025 August https://doi.org/10.3847/1538-3881/addd17

Eleven New Transiting Brown Dwarfs and Very-low-mass Stars from TESS

Noah Vowell[1,2], Joseph E. Rodriguez[1], David W. Latham[2], Samuel N. Quinn[2], Jack Schulte[1], Jason D. Eastman[2], Allyson Bieryla[2], Khalid Barkaoui[3,4,5], David R. Ciardi[6], Karen A. Collins[2], Eric Girardin[7], Guillaume Hébrard[8,9], Elisabeth Heldridge[10], Marziye Jafariyazani[11], Brooke Kotten[12], Luigi Mancini[13,14,15], Felipe Murgas[16,17], Norio Narita[16,18,19], D. J. Radford[20], Howard M. Relles[2], Avi Shporer[21], Melinda Soares-Furtado[22], Ivan A. Strakhov[23], Carl Ziegler[24], Isabelle Boisse[25,26], César Briceño[27], Michael L. Calkins[2], Catherine A. Clark[6], Kevin I. Collins[28], Jerome de Leon[5,18], Gilbert A. Esquerdo[2], Sergio B. Fajardo-Acosta[29], Thierry Forveille[30], Akihiko Fukui[16,18], Cristilyn N. Watkins[2], Ruixuan He[10], Neda Heidari[8], Keith Horne[31], Jon M. Jenkins[32], Andrew W. Mann[33], Luca Naponiello[15], Enric Palle[16,17], Richard P. Schwarz[2], S. Seager[21,34,35], John Southworth[36], Gregor Srdoc[37], Jonathan J. Swift[10], and Joshua N. Winn[38]

[1] Center for Data Intensive and Time Domain Astronomy, Department of Physics and Astronomy, Michigan State University, East Lansing, MI 48824, USA; vowellno@msu.edu
[2] Center for Astrophysics | Harvard & Smithsonian, 60 Garden Street, Cambridge, MA 02138, USA
[3] Astrobiology Research Unit, Université de Liége, 19C Allée du 6 Août, 4000 Liége, Belgium
[4] Department of Earth, Atmospheric and Planetary Science, Massachusetts Institute of Technology, 77 Massachusetts Avenue, Cambridge, MA 02139, USA
[5] Instituto de Astrofísica de Canarias (IAC), Calle Vía Láctea s/n, 38200, La Laguna, Tenerife, Spain
[6] NASA Exoplanet Science Institute-Caltech/IPAC, Pasadena, CA 91125, USA
[7] Grand Pra Observatory, 1984 Les Hauderes, Switzerland
[8] Institut d'astrophysique de Paris, UMR7095 CNRS, Université Pierre & Marie Curie, 98bis boulevard Arago, 75014 Paris, France
[9] Observatoire de Haute-Provence, CNRS, Université d'Aix-Marseille, 04870 Saint-Michel-l'Observatoire, France
[10] The Thacher School, 5025 Thacher Road, Ojai, CA 93023, USA
[11] SETI Institute, Mountain View, CA 94043 USA/NASA Ames Research Center, Moffett Field, CA 94035, USA
[12] Department of Astronomy, University of Michigan, Ann Arbor, MI 48109, USA
[13] Department of Physics, University of Rome "Tor Vergata," Via della Ricerca Scientifica 1, I-00133, Rome, Italy
[14] Max Planck Institute for Astronomy, Königstuhl 17, D-69117, Heidelberg, Germany
[15] INAF – Osservatorio Astrofisico di Torino, via Osservatorio 20, I-10025, Pino Torinese, Italy
[16] Instituto de Astrofísica de Canarias (IAC), E-38205 La Laguna, Tenerife, Spain
[17] Departamento de Astrofísica, Universidad de La Laguna (ULL), E-38206 La Laguna, Tenerife, Spain
[18] Komaba Institute for Science, The University of Tokyo, 3-8-1 Komaba, Meguro, Tokyo 153-8902, Japan
[19] Astrobiology Center, 2-21-1 Osawa, Mitaka, Tokyo 181 8588, Japan
[20] Brierfield Observatory, Bowral, NSW 2576, Australia
[21] Department of Physics and Kavli Institute for Astrophysics and Space Research, Massachusetts Institute of Technology, Cambridge, MA 02139, USA
[22] Department of Astronomy, University of Wisconsin-Madison, 475 N. Charter Street, Madison, WI 53706, USA
[23] Sternberg Astronomical Institute, Lomonosov Moscow State University, Universitetsky pr. 13, Moscow 119234, Russia
[24] Department of Physics, Engineering and Astronomy, Stephen F. Austin State University, 1936 North Street, Nacogdoches, TX 75962, USA
[25] Laboratoire d'astrophysique de Marseille, Univ. de Provence, UMR6110 CNRS, 38 r. F. Joliot Curie, 13388 Marseille cedex 13, France
[26] Aix Marseille Univ, CNRS, CNES, LAM, Marseille, France
[27] SOAR Telescope/NSF NOIRLab, Casilla 603, La Serena, Chile
[28] George Mason University, 4400 University Drive, Fairfax, VA 22030, USA
[29] Caltech/IPAC, Mail Code 100-22, Pasadena, CA 91125, USA
[30] Université Grenoble Alpes, CNRS, IPAG, 38000 Grenoble, France
[31] SUPA Physics and Astronomy, University of St. Andrews, Fife, KY16 9SS, UK
[32] NASA Ames Research Center, Moffett Field, CA 94035, USA
[33] Department of Physics and Astronomy, The University of North Carolina at Chapel Hill, Chapel Hill, NC 27599-3255, USA
[34] Department of Earth, Atmospheric and Planetary Sciences, Massachusetts Institute of Technology, Cambridge, MA 02139, USA
[35] Department of Aeronautics and Astronautics, Massachusetts Institute of Technology, 77 Massachusetts Avenue, Cambridge, MA 02139, USA
[36] Astrophysics Group, Keele University, Staffordshire, ST5 5BG, UK
[37] Kotizarovci Observatory, Sarsoni 90, 51216 Viskovo, Croatia
[38] Department of Astrophysical Sciences, Princeton University, Princeton, NJ 08544, USA

Received 2025 January 16; revised 2025 May 8; accepted 2025 May 19; published 2025 July 4

Abstract

We present the discovery of 11 new transiting brown dwarfs (BDs) and low-mass M dwarfs from NASA's Transiting Exoplanet Survey Satellite (TESS) mission: TOI-2844, TOI-3122, TOI-3577, TOI-3755, TOI-4462, TOI-4635, TOI-4737, TOI-4759, TOI-5240, TOI-5467, and TOI-5882. They consist of five BD companions and six very-low-mass stellar companions ranging in mass from 25 M_J to 128 M_J. We used a combination of photometric time-series, spectroscopic, and high-resolution imaging follow-up as a part of the TESS Follow-up Observing Program (or TFOP) to characterize each system. With over 50 transiting BDs confirmed, we now have a large enough sample to directly test different formation and evolutionary scenarios. We provide a renewed perspective on the transiting "brown dwarf desert" and its role in differentiating between planetary and stellar formation mechanisms. Our analysis of the eccentricity distribution for the transiting BD sample does not support previous claims of a transition between planetary and stellar formation at $\sim 42\,M_{\rm J}$. We also contribute a first look into the metallicity distribution of transiting companions in the range 7–150 $M_{\rm J}$, showing that this does not support a $\sim 42\,M_{\rm J}$ transition too. Finally, we also detect a significant lithium absorption feature in one of the BD hosts (TOI-5882). However, we determine that the host star is likely old based on rotation, kinematic, and photometric mdeasurements. We therefore claim that TOI-5882 may be a candidate for planetary engulfment.

Unified Astronomy Thesaurus concepts: Brown dwarfs (185); Exoplanets (498); M dwarf stars (982); Transits (1711); Radial velocity (1332)

Materials only available in the online version of record: machine-readable table

1. Introduction

Since the launch of NASA's Transiting Exoplanet Survey Satellite (TESS) in 2018 (G. R. Ricker et al. 2015), the number of brown dwarfs (BDs) known to transit their host stars has increased rapidly from just 16 systems to >50. These BDs, which are defined as objects within the mass range of 13–80 $M_{\rm J}$, fuse only deuterium in their cores. This differentiates them from planets, which undergo no fusion, and stars, which ignite hydrogen fusion. However, the deuterium- and hydrogen-burning limits have been shown to be less clear than this definition would imply. D. S. Spiegel et al. (2011) showed that the lower limit varies from 11 to 16 $M_{\rm J}$, while I. Baraffe et al. (2003) showed that hydrogen fusion can ignite between 75 and 80 $M_{\rm J}$. The spread in both of these estimates can be explained by variation in the chemical composition and formation conditions of the BD. While these definitions provide insight into the physical processes taking place in BD interiors, they offer little insight into how they form.

Reframing our perspective on BDs into one motivated by formation and evolution has long been advocated for by some members of the BD community (A. S. Burrows 2014; G. Chabrier et al. 2014; T. W. Carmichael et al. 2021), where objects would be distinguished based on whether they form through a planet-like or a star-like formation mechanism. BDs forming like planets would undergo a core-accretion pathway (J. B. Pollack et al. 1996), commonly referred to as a "bottom-up" approach. The star-like BDs, on the other hand, would form via direct gravitational collapse, or "top-down," which can happen either within the circumstellar disk or at the core scale (F. C. Adams et al. 1989; M. R. Bate 2012; K. Kratter & G. Lodato 2016). Differentiating between these two formation pathways remains challenging, since it is unclear under what conditions each mechanism dominates, and whether there are any observable parameters that could distinguish them. Fortunately, in the era of TESS we have begun to accumulate transiting BDs en masse, allowing us to pursue the question of BD formation from a different perspective. This budding population of transiting BDs is particularly enticing for studying BD formation because it provides a complementary, and in many cases more complete, understanding of BDs compared to previously studied objects, which have primarily been discovered via direct imaging or radial velocity (RV) techniques. The transiting population serves as a complementary data set to these other populations because transits provide a model-independent measurement of BD radii, a property which often can only be otherwise inferred with evolutionary models based on the observed spectrum and luminosity. This measurement is vital because BDs tend to contract with age, while also decreasing in size as mass increases (A. Burrows et al. 2001; I. Baraffe et al. 2003; D. Saumon & M. S. Marley 2008; M. W. Phillips et al. 2020). Thus, there exists a degeneracy between mass, radius, and age for BDs, making it difficult to test the substellar models with observed systems unless all three variables can be measured. These transiting systems provide direct, independent measurements on two of these degenerate parameters, and in cases where the host star's age can be precisely determined all three (e.g., E. Gillen et al. 2017; G. Nowak et al. 2017; T. J. David et al. 2019; N. Vowell et al. 2023).

This rapidly growing population of transiting BDs also allows us to revisit the longstanding idea of the so-called "brown dwarf desert." Prior work has shown a dearth of BDs orbiting main-sequence host stars with semimajor axes <5 au. (G. W. Marcy et al. 1997; D. W. Latham et al. 1998). B. Ma & J. Ge (2014) refined our understanding of the BD desert by investigating the population of all published BDs discovered with the RV method at the time. Here they found that the "driest land" of the desert lies between $35 < m \sin i < 55\,M_{\rm J}$ and with period $P < 100$ days. The authors attribute this feature to being a result of different formation mechanisms dominating in different mass regimes. Namely, that stellar binary formation is responsible for the systems with BD companions $> 42\,M_{\rm J}$ while formation in the protoplanetary disk explains the systems with BDs $< 42\,M_{\rm J}$. However, the sample in this study with period $P < 100$ days was quite small, at only 25 BDs. Furthermore, by virtue of being a RV study, it was restricted to only probing $m \sin i$ rather than the BD mass directly, unable to break the $\sin i$ degeneracy in most cases, a complication that the transiting population does not have.

As this population of transiting BDs expanded in the era of space-based transit surveys, several new discoveries noted an "oasis" forming in the desert (T. W. Carmichael et al. 2020; J. Šubjak et al. 2020; B. A. Henderson et al. 2024a) with new transiting systems beginning to populate the driest region of the desert noted by B. Ma & J. Ge (2014). With the new discoveries presented in this work, the transiting BD population now exceeds 50 systems, more than double the size of the population B. Ma & J. Ge (2014) had access to, opening the door for a reevaluation of the BD desert from a new perspective. Hence, in this paper we present the discovery of 11 new transiting companions from NASA's TESS mission. Six of these systems are BDs, with three lying within the B. Ma & J. Ge (2014) defined "driest" region of the BD desert. We confirmed the remaining six non-BD companions as very-low-mass stars $<150\,M_{\rm J}$. In Section 2 of this manuscript, we present all the observations collected for each system in this work. Section 3 details our analysis of each system using `EXOFASTv2` (J. Eastman et al. 2013; J. D. Eastman et al. 2019). In Section 4, we provide a discussion on how these new systems fit into the population as a whole with a renewed perspective on the BD desert. We also discuss a detection of

Table 1
Literature and Measured Properties

		TOI-2844	TOI-3122	TOI-3577	TOI-3755	Source
Other identifiers						
	TESS Input Catalog	TIC 387342052	TIC 61117473	TIC 396133015	TIC 281196902	
	TYCHO-2	TYC 771-367-1	TYC 6773-1-1	TYC 3608-647-1	⋯	
	2MASS	J07204878+1301073	J15074899–2809237	J21482300+4820042	J04385936+6640161	
	Gaia DR3	3166196736096450816	6212565847439064192	1977894600881987328	483359575160953728	
Astrometric Parameters						
$\alpha_{\rm J2000}$[a]	R.A. (hh:mm:ss)	07:20:48.78	15:07:48.99	21:48:23.01	04:38:59.37	(1)
$\delta_{\rm J2000}$[a]	decl. (deg:arcmin:arcsec)	13:01:07.4	−28:09:23.8	48:20:04.4	66:40:16.2	(1)
μ_α	Gaia DR3 proper motion in R.A. (mas yr^{-1})	-2.992 ± 0.016	-13.329 ± 0.015	5.052 ± 0.011	-11.614 ± 0.007	(1)
μ_δ	Gaia DR3 proper motion in decl. (mas yr^{-1})	-4.906 ± 0.016	-0.501 ± 0.013	-33.472 ± 0.011	11.407 ± 0.009	(1)
π	Gaia DR3 parallax (mas)	1.4262 ± 0.0137	1.9337 ± 0.0147	2.3184 ± 0.011	3.0749 ± 0.0104	(1)
$v \sin i_\star$	Projected rotational velocity (km s^{-1})	60.8 ± 2.6	23.2 ± 5.1	10.3 ± 0.5	5.1 ± 0.5	(2)
Photometric Parameters						
G	Gaia G mag	11.87 ± 0.02	12.52 ± 0.02	11.75 ± 0.02	12.62 ± 0.02	(1)
$G_{\rm BP}$	Gaia $G_{\rm BP}$ mag	12.08 ± 0.02	12.835 ± 0.02	12.07 ± 0.02	13.06 ± 0.02	(1)
$G_{\rm RP}$	Gaia $G_{\rm RP}$ mag	11.52 ± 0.02	12.05 ± 0.02	11.26 ± 0.02	12.01 ± 0.02	(1)
T	TESS mag	11.583 ± 0.007	12.123 ± 0.008	11.321 ± 0.006	12.079 ± 0.006	(3)
J	2MASS J mag	11.168 ± 0.022	11.515 ± 0.026	10.638 ± 0.023	11.316 ± 0.024	(4)
H	2MASS H mag	10.967 ± 0.027	11.277 ± 0.025	10.381 ± 0.03	10.966 ± 0.028	(4)
K	2MASS K mag	10.927 ± 0.021	11.207 ± 0.024	10.318 ± 0.020	10.876 ± 0.022	(4)
W1	WISE W1 mag	10.90 ± 0.03	11.05 ± 0.03	10.24 ± 0.03	10.82 ± 0.03	(5)
W2	WISE W2 mag	10.93 ± 0.03	11.07 ± 0.03	10.27 ± 0.03	10.87 ± 0.03	(5)
W3	WISE W3 mag	10.987 ± 0.143	11.147 ± 0.155	10.298 ± 0.046	10.651 ± 0.093	(5)
		TOI-4462	TOI-4635	TOI-4737	TOI-4759	Source
Other identifiers						
	TESS Input Catalog	TIC 76420654	TIC 337129672	TIC 142532090	TIC 49705089	
	TYCHO-2	TYC 2635-1030-1	⋯	⋯	⋯	
	2MASS	J18184078+3615175	J02143112+0804481	J06533851-1326106	J06234422-2401288	
	Gaia DR3	4605954852723545088	2521579495665163008	2949605211853441664	2936390357694302336	
Astrometric Parameters						
$\alpha_{\rm J2000}$[a]	R.A. (hh:mm:ss)	18:18:40.78	02:14:31.26	06:53:38.51	06:23:44.23	(1)
$\delta_{\rm J2000}$[a]	decl. (deg:arcmin:arcsec)	36:15:17.5	08:04:45.3	-13:26:10.7	-24:01:28.9	(1)
μ_α	Gaia DR3 proper motion in R.A. (mas yr^{-1})	6.959 ± 0.038	122.150 ± 0.026	11.332 ± 0.013	0.634 ± 0.009	(1)
μ_δ	Gaia DR3 proper motion in decl. (mas yr^{-1})	-3.105 ± 0.045	-203.829 ± 0.019	-20.658 ± 0.014	7.847 ± 0.012	(1)
π	Gaia DR3 parallax (mas)	2.5184 ± 0.0365	13.3018 ± 0.0238	1.7169 ± 0.0132	1.3243 ± 0.0107	(1)
$v \sin i_\star$	Projected rotational velocity (km s^{-1})	18.6 ± 0.4	3.5 ± 1.1	5.1 ± 0.6	13.4 ± 0.6	(2)
Photometric Parameters						
G	Gaia G mag	10.88 ± 0.02	11.32 ± 0.02	12.43 ± 0.02	12.73 ± 0.02	(1)
$G_{\rm BP}$	Gaia $G_{\rm BP}$ mag	11.17 ± 0.02	11.99 ± 0.02	12.78 ± 0.02	13.10 ± 0.02	(1)
$G_{\rm RP}$	Gaia $G_{\rm RP}$ mag	10.39 ± 0.02	10.53 ± 0.02	11.93 ± 0.02	12.20 ± 0.02	(1)
T	TESS mag	10.445 ± 0.006	10.445 ± 0.006	11.992 ± 0.006	12.263 ± 0.007	(3)
J	2MASS J mag	9.882 ± 0.020	9.565 ± 0.025	11.355 ± 0.024	11.596 ± 0.022	(4)
H	2MASS H mag	9.585 ± 0.020	8.987 ± 0.028	11.057 ± 0.025	11.325 ± 0.025	(4)
K	2MASS K mag	9.513 ± 0.020	8.854 ± 0.025	10.988 ± 0.025	11.21 ± 0.026	(4)
W1	WISE W1 mag	9.46 ± 0.03	8.70 ± 0.03	10.93 ± 0.03	11.12 ± 0.03	(5)
W2	WISE W2 mag	9.49 ± 0.03	8.74 ± 0.03	10.97 ± 0.03	11.15 ± 0.03	(5)
W3	WISE W3 mag	9.410 ± 0.033	8.696 ± 0.030	10.960 ± 0.107	11.166 ± 0.107	(5)
		TOI-5240	TOI-5467	TOI-5882		Source
Other identifiers						
	TESS Input Catalog	TIC 40055053	TIC 83275782	TIC 232941965		
	TYCHO-2	TYC 2663-268-1	⋯	TYC 2695-1754-1		
	2MASS	J19322010+3456254	J06173449+2826431	J20473329+3444151		
	Gaia DR3	2046792606517797632	3433414139371114368	1869489729418662528		

Table 1
(Continued)

		TOI-2844	TOI-3122	TOI-3577	TOI-3755	Source
Astrometric Parameters						
α_{J2000}[a]	R.A. (hh:mm:ss)	19:32:20.11	06:17:34.49	20:47:33.29		(1)
δ_{J2000}[a]	decl. (deg:arcmin:arcsec)	34:56:25.4	28:26:43.1	34:44:15.2		(1)
μ_α	Gaia DR3 proper motion in R.A. (mas yr^{-1})	-0.414 ± 0.011	0.599 ± 0.016	-14.084 ± 0.014		(1)
μ_δ	Gaia DR3 proper motion in decl. (mas yr^{-1})	0.502 ± 0.012	-13.726 ± 0.012	-17.246 ± 0.017		(1)
π	Gaia DR3 parallax (mas)	0.9894 ± 0.0114	1.7558 ± 0.0138	2.3859 ± 0.0144		(1)
$v \sin i_\star$	Projected rotational velocity (km s^{-1})	32.8 ± 1.3	31.2 ± 0.4	7.3 ± 0.5		(2)
Photometric Parameters						
G	Gaia G mag	11.92 ± 0.02	12.25 ± 0.02	11.11 ± 0.02		(1)
G_{BP}	Gaia G_{BP} mag	12.09 ± 0.02	12.56 ± 0.02	11.47 ± 0.02		(1)
G_{RP}	Gaia G_{RP} mag	11.63 ± 0.02	11.78 ± 0.02	10.58 ± 0.02		(1)
T	TESS mag	11.692 ± 0.009	11.842 ± 0.006	10.634 ± 0.006		(3)
J	2MASS J mag	11.307 ± 0.021	11.255 ± 0.021	9.988 ± 0.020		(4)
H	2MASS H mag	11.176 ± 0.022	11.011 ± 0.023	9.736 ± 0.020		(4)
K	2MASS K mag	11.154 ± 0.020	10.947 ± 0.020	9.615 ± 0.020		(4)
W1	WISE W1 mag	11.14 ± 0.03	10.90 ± 0.03	9.57 ± 0.03		(5)
W2	WISE W2 mag	11.16 ± 0.03	10.91 ± 0.03	9.60 ± 0.03		(5)
W3	WISE W3 mag	10.928 ± 0.096	10.952 ± 0.144	9.662 ± 0.055		(5)

Notes. The uncertainties of the photometric measurements have a systematic floor applied that is usually larger than the reported catalog errors.

[a] R.A. and decl. are in epoch J2000. The coordinates come from Vizier where the Gaia R.A. and decl. have been processed and corrected to J2000 from epoch J2016.

Sources: (1) Gaia Collaboration et al. (2023); (2) Section 2.3; (3) K. G. Stassun et al. (2019); (4) R. M. Cutri et al. (2003); M. F. Skrutskie et al. (2006); (5) E. L. Wright et al. (2010); R. M. Cutri et al. (2012).

lithium (Li) in the host star of the BD companions presented here (TOI-5882). Finally, we present our conclusions in Section 5.

2. Observations

In the following subsections, we present all observations collected and analyzed for each target in this sample. To briefly summarize, each target has a suite of observations that serve to characterize the host star and/or companion and rule out false-positive scenarios. Generally, these observations include archival multiband observations from various ground-based missions, time-series photometry from both space- and ground-based telescopes, spectroscopy, and high-resolution imaging. See Table 1 for the relevant results of the archival data associated with each system.

2.1. TESS Photometry

Each system presented here initially showed signs of an orbiting companion via transits detected by TESS. TESS has a mosaic of four CCD cameras each with a 24° × 24° field of view, and a pixel size of 21″. In combination, this makes the TESS field of view 24° × 96° for each sector, which is observed for approximately 27 days before moving to a new sector of sky. TESS observes at a 2 s cadence, and in the TESS prime mission the data were processed into 2 minutes stacks for select stars, with the rest of the field being processed at 30 minutes cadence. This prime mission observed >80% of the entire sky, with the largest gaps in coverage occurring near the ecliptic plane. As TESS transitioned to its first, and now second, extended missions it continues to observe even more of the ecliptic plane. In this second extended mission, most preselected targets are now processed at 120 s, while a smaller number are processed at 20 s cadence. Full-frame images are processed at 200 s.

The systems presented here were observed by TESS between Sectors 6–76 with cadences ranging from 30 minutes in the prime mission to as low as 2 minutes in the extended mission. The TESS data were originally downloaded and reduced using both the TESS Science Processing Operations Center (SPOC) pipeline (J. M. Jenkins et al. 2016) and the MIT Quick-Look Pipeline (QLP; C. X. Huang et al. 2020a, 2020b; M. Kunimoto et al. 2021). The initial detection of a transit-like signal was discovered and vetted by the faint-star QLP search (M. Kunimoto et al. 2022) for 10 out the 12 systems presented in this paper. The remaining two, TOI-4462 and TOI-4635, were initially detected by the QLP and SPOC pipelines, respectively, and then vetted by the TESS Science Office. The diagnostic tests described in J. D. Twicken et al. (2018) were used to evaluate whether the transit-like signal is indeed Keplerian. Upon passing, each system was designated as a TESS Object of Interest (TOI; N. M. Guerrero et al. 2021). While both the QLP and SPOC pipelines correct for contamination by known nearby stars, we choose to use the SPOC light curves with the shortest cadence in our analysis wherever possible for consistency. See Table 2 for full details on the sectors, cadence, and pipeline used for each source. It should be noted that all QLP light curves are processed from the full-frame images. The TESS-SPOC (D. A. Caldwell et al. 2020) light curves are produced by the SPOC on a best-effort basis under the leadership of Doug Caldwell, the PI, and delivered as high-level science products to the Mikulski Archive for Space Telescopes (MAST) rather than as part of the official mission data products produced by the SPOC.

Table 2
Summary of Observations from TESS

Target	TESS Sector	Cadence (s)	Pipeline
TOI-2844	7	1800	TESS-SPOC
…	33	600	TESS-SPOC
…	44	600	TESS-SPOC
…	45	600	TESS-SPOC
…	46	600	TESS-SPOC
…	71	120	SPOC
…	72	120	SPOC
TOI-3122	11	1800	QLP
…	38	600	QLP
…	65	120	SPOC
TOI-3577	8	1800	QLP
…	56	120	SPOC
…	76	120	SPOC
TOI-3755	19	1800	TESS-SPOC
…	59	120	SPOC
…	73	120	SPOC
TOI-4462	26	1800	TESS-SPOC
…	40	600	TESS-SPOC
…	53	600	TESS-SPOC
…	54	600	TESS-SPOC
…	74	120	SPOC
TOI-4635	42	120	SPOC
…	43	120	SPOC
…	70	120	SPOC
…	71	120	SPOC
TOI-4737	6	1800	TESS-SPOC
…	7	1800	QLP
…	33	600	TESS-SPOC
TOI-4759	6	1800	QLP
…	33	600	QLP
TOI-5240	14	1800	QLP
…	40	600	QLP
…	41	600	TESS-SPOC
…	54	600	QLP
…	55	600	QLP
…	74	120	SPOC
…	75	120	SPOC
TOI-5467	43	600	TESS-SPOC
…	44	600	TESS-SPOC
…	45	600	TESS-SPOC
…	71	120	TESS-SPOC
…	72	120	TESS-SPOC
TOI-5882	15	1800	TESS-SPOC
…	41	600	TESS-SPOC
…	55	600	TESS-SPOC
…	75	120	SPOC

We downloaded the individual light curves from the MAST using the `lightkurve` package (Lightkurve Collaboration et al. 2018).[39] We then removed any long-term variability (both stellar and instrumental) by fitting a spline to the flux and dividing the light curve by the best-fitting spline model. We used the `Keplerspline` package[40] for this process as described in A. Vanderburg & J. A. Johnson (2014). We remove most of the out-of-transit data, electing to keep just one transit duration of baseline on either side of the transit.

2.2. Ground-based Time-series Photometry

In order to confirm that the signal observed by TESS is on target, not originating from a nearby eclipsing binary that is blended with the target star, we gathered ground-based time-series photometry of each system as the companion transited its host star. Since TESS has a relatively large pixel scale (21″ per pixel), the shallow eclipses we measured, which are consistent with roughly 1 R_J, can be easily mimicked when a different, nearby eclipsing binary happens to fall on the same photometric aperture as the target star. The much deeper eclipses of the nearby eclipsing binary become diluted by the target star to mimic a much shallower event. Seeing-limited ground-based telescopes can have a much higher angular resolution than TESS, typically 1″–2″, and therefore can confirm that the signal is on target, thereby ruling out nearby eclipsing binaries at all but the closest separations. They also have the benefit of observing in multiple wavelengths to confirm that the transit-like signal is achromatic. This is helpful because the eclipse depth of an eclipsing binary is nearly always wavelength dependent since the occulting body cannot be treated as a nonluminous sphere. We also note here, that while six of the companions presented herein are low-mass M dwarfs, and hence are eclipsing binaries themselves, they are so low in mass that we can still treat them as black spheres since they contribute negligibly to the overall flux of the system (D. J. Stevens et al. 2018). This process not only rules out the nearby eclipsing binary false positive, but also serves to refine the ephemerides of systems in which these data are able to extend the photometric baseline.

The observations for these systems were collected through the TESS Follow-up Observing Program (TFOP; K. A. Collins et al. 2018) from various observatories as shown in Table 3. The Las Cumbres Observatory Global Telescope (LCOGT; T. M. Brown et al. 2013) was responsible for 14 light curves from the following sites: McDonald Observatory (McD), Teide Observatory (TEID), South African Astronomical Observatory (SAAO), and Cerro Tololo Inter-American Observatory (CTIO). The remaining light curves were contributed by the following facilities: Calar Alto Observatory, Brierfield Observatory, the Telescopio Carlos Sánchez (TCS) at Teide Observatory, Grand-Pra (GdP) Observatory, Thacher Observatory (J. J. Swift et al. 2022), KeplerCam at the Fred Lawrence Whipple Observatory (FLWO), and the Acton Sky Portal.

All data sets, except for the observations of TOI-3577 from MuSCAT2, were reduced and their light curves extracted using `AstroImageJ` (AIJ; K. A. Collins et al. 2017). To do this, we use AIJ’s multi-aperture photometry tool using at least five similarly bright comparison stars. We use AIJ’s built-in transit fitting tool to assess the quality of the data and determine detrending parameters. Generally, we only detrend against the parameters that strongly correlate with the apparent brightness of the companion stars as they change over the course of the night. We choose to adopt detrending only when the Bayesian information criterion of AIJ’s transit-only fit significantly favors the detrended model. The detrending parameters used for each light curve can be found in Table 3. See Section D in the Appendix of K. A. Collins et al. (2017) for a detailed description of each detrending parameter. Finally, we normalized the data to the out-of-transit baseline and incorporated each light curve (with detrending) into our global fitting process (see Section 3).

---

[39] https://github.com/lightkurve/lightkurve

[40] https://github.com/avanderburg/keplerspline

Table 3
Follow-up Observations

TIC ID	TOI	Telescope	Camera	Observation Date (UT)	Telescope Size (m)	Filter	Pixel Scale (arcsec)	Exposure Time (s)	Detrend Params
387342052	2844	LCO-McD	QHY600	2023 Apr 5	0.35	*i*’	0.7	135	Air mass
		Zeiss Calar Alto	iKon-XL 230	2023 Nov 21	1.23	*R*	0.314	90	None
		LCO-TEID	Sinistro	2023 Nov 29	1.0	*i*’	0.389	19	None
61117473	3122	Brierfield	Moravian 16803	2023 May 15	0.36	*R*	0.735	180	Air mass
396133015	3577	TCS	MuSCAT2	2023 Jul 16	1.52	*g*’	0.44	10	None
		TCS	MuSCAT2	2023 Jul 16	1.52	*r*’	0.44	5	None
		TCS	MuSCAT2	2023 Jul 16	1.52	*i*’	0.44	5	None
		TCS	MuSCAT2	2023 Jul 16	1.52	z_s	0.44	10	None
281196902	3755	GdP	FLI4710	2022 Mar 3	0.4	*i*’	0.73	90	None
		Thacher CDK-700	Teledyne PIXIS	2023 Oct 18	0.7	*r*’	0.608	40	None
76420654	4462	FLWO	KeplerCam	2024 Mar 19	1.2	*i*’	0.672	6	Air mass
		LCO-TEID	Sinistro	2024 Apr 3	1.0	*i*’	0.389	38	tot_C_cnts
337129672	4635	LCO-SAAO	Sinistro	2023 Nov 22	1.0	*z*’	0.389	37	None
		LCO-CTIO-fa04	Sinistro	2023 Dec 5	1.0	*z*’	0.389	37	None
		LCO-CTIO-fa15	Sinistro	2023 Dec 5	1.0	*z*’	0.389	37	Air mass
142532090	4737	LCO-TEID	Sinistro	2023 Nov 26	1.0	*i*’	0.389	33	None
		LCO-CTIO	Sinistro	2023 Dec 6	1.0	*i*’	0.389	33	None
		LCO-SAAO	Sinistro	2023 Dec 24	1.0	*i*’	0.389	33	Air mass
49705089	4759	LCO-SAAO-fa06	Sinistro	2024 Feb 5	1.0	*i*’	0.389	44	Air mass
		LCO-SAAO-fa14	Sinistro	2024 Feb 5	1.0	*i*’	0.389	44	None
40055053	5240	LCO-TEID	Sinistro	2023 Aug 2	1.0	*i*’	0.389	26	None
83275782	5467	FLWO	KeplerCam	2023 Mar 4	1.2	*i*’	0.672	15	Air mass
		Acton Sky Portal	SBIG A4710	2023 Mar 20	0.36	*r*’	1.0	20	Air mass
		LCO-McD	Sinistro	2023 Oct 13	1.0	*i*’	0.389	29	tot_C_cnts
232941965	5882	LCO-McD	Sinistro	2023 Jun 16	1.0	*z*’	0.389	45	None

Note. All light curves are available on ExoFOP (https://exofop.ipac.caltech.edu).

Our follow-up observations of TOI-3577 were taken by MuSCAT2 on the TCS from Teide Observatory in Tenerife, Spain (N. Narita et al. 2019). MuSCAT2 is a multiband imager with four cameras, each with a field of view of $7'.4 \times 7'.4$. This setup allows for simultaneous observation in multiple bands, which in our case were the g', r', i', and z_s bands. These data were reduced by the dedicated MuSCAT2 pipeline (H. Parviainen et al. 2019), and incorporated into our global fit.

2.3. Spectroscopy

We collected spectroscopic observations for each system to measure the mass and eccentricity of their companions while also further ruling out the false-positive scenario of nearby eclipsing binaries. While several of the systems presented here have companions above the hydrogen-burning boundary, and thus are eclipsing binaries themselves, none of them have companions that are bright enough to be detected photometrically or spectroscopically. Hence, they are all single-lined spectroscopic binaries. Any potential nearby eclipsing binaries (both bound and unbound) that cannot be ruled out by ground-based photometry can be ruled out by spectroscopy within the angular diameter of the fiber. These are ruled out by the fact that the companions presented here are significantly more massive than their giant planet counterparts. The Doppler motion of the host stars’ spectral lines is too large to be mimicked by a nearby eclipsing binary without resolving a secondary set of spectral features.

We obtained spectroscopic measurements for each system in this sample via the Tillinghast Reflector Échelle Spectrograph (TRES) on the 1.5 m Tillinghast Reflector telescope at the Fred Lawrence Whipple Observatory on Mt. Hopkins, Arizona. The TRES instrument is a fiber-fed, échelle spectrograph with a resolving power of 44,000. We reduced the spectra according to L. A. Buchhave et al. (2010) and analyzed each observation with the Stellar Parameter Classification (SPC) tool (L. A. Buchhave et al. 2012) in order to measure the metallicity, effective temperature, surface gravity, and projected rotational velocity of the star. We incorporated the average metallicity for each system into our analysis as a Gaussian prior in our global fits (see Section 3). We did not incorporate the effective temperature or surface gravity measurements from SPC as priors because these quantities are better constrained by the fit itself. This is due to the fact that `EXOFASTv2` simultaneously models the spectral energy distribution (SED), companion’s transit, and stellar evolutionary models (J. D. Eastman et al. 2023)

Finally, we derived the RVs according to the methods described in S. N. Quinn et al. (2012), except that we do not cross-correlate against a template spectrum. Instead, we create a high-signal-to-noise ratio (S/N), median-combined observed spectrum that we cross-correlate with each individual spectrum. See Table 4 for a sample RV point for each system (the full table of RVs is available in machine-readable form in the online journal).

Table 4
One Representative RV Measurement for Each System

Target	BJD_{TDB}	RV ($m\ s^{-1}$)	σ_{RV} ($m\ s^{-1}$)	Spectrograph
TOI-2844	2459528.8676	−6696	1791	TRES
TOI-3122	2459651.9406	14841	145	TRES
TOI-3577	2459395.9184	52	70	TRES
TOI-3755	2459477.9662	−8617	31	TRES
TOI-4462	2459468.6623	944	76	TRES
TOI-4635	2459556.7367	6170	19	TRES
TOI-4737	2459583.9325	2529	65	TRES
TOI-4759	2459623.7415	−64	53	TRES
TOI-5240	2459681.9612	20204	375	TRES
TOI-5467	2459697.6358	−237	352	TRES
TOI-5882	2459899.6240	108	55	TRES
TOI-5882	2459930.2705	−22361.2	12.4	SOPHIE

(This table is available in its entirety in machine-readable form in the online article.)

2.3.1. SOPHIE Spectroscopy

We complement the TRES data with SOPHIE observations of TOI-5882. SOPHIE is a stabilized échelle spectrograph dedicated to high-precision RV measurements at the 1.93 m telescope of the Observatoire de Haute-Provence, France (S. Perruchot et al. 2008; F. Bouchy et al. 2009, 2013). We used its high-resolution mode (resolving power $R = 75{,}000$) and the fast readout of its CCD.

Removing a few observations with low accuracy, we have a data set of 21 SOPHIE measurements of TOI-5882 secured from 2022 December to 2024 July. Exposure times ranged between 5 and 37 minutes, allowing S/Ns between 14 and 40 to be reached per pixel at 550 nm.

The RVs were extracted with the SOPHIE pipeline, as presented by F. Bouchy et al. (2009) and refined by N. Heidari et al. (2024, 2025). That procedure includes corrections for bad pixels, cosmic rays, and charge transfer inefficiency of the CCD, as well as sky background and instrumental drifts. It derives cross-correlation functions (CCFs) from a numerical mask, then fits the CCFs by Gaussians to derive the RVs (A. Baranne et al. 1996; F. Pepe et al. 2002). One sample measurement is reported in Table 4.

2.4. High-resolution Imaging

While ground-based transits rule out nearby eclipsing binaries at most scales, if another source is close enough to the target star it may be blended both in TESS and from the ground. Therefore, to verify that there is no contamination at these very small separations, and in order to detect any potentially bright companions, we utilized high-resolution imaging. We employed both adaptive optics (AO) and speckle imaging instruments to obtain our high-resolution images for these systems.

We used the ShARCS and PHARO instruments for AO imaging. The ShARCS instrument is on the Shane 3.0 m telescope located at Lick Observatory (R. Kupke et al. 2012; D. Gavel et al. 2014; R. McGurk et al. 2014). The PHARO instrument is on the Palomar Hale 5 m telescope at Palomar Observatory (T. L. Hayward et al. 2001). For our speckle observations, we used the following telescopes and instruments: HRCam on the Southern Astrophysical Research (SOAR) 4.1 m telescope at CTIO (A. Tokovinin 2018; C. Ziegler et al. 2020), the NN-EXPLORE Exoplanet Stellar Speckle Imager (NESSI; N. J. Scott et al. 2018) on the WIYN 3.5 m telescope at Kitt Peak Observatory, the Speckle Polarimeter on the 2.5 m telescope at the Caucasian Mountain Observatory of the Sternberg Astronomical Institute (SAI) at Lomonosov Moscow State University, and the Zorro instrument on the Gemini-South 8 m telescope. The Speckle Polarimeter used an Andor iXon 897 electron-multiplying CCD for the observation of TOI-3755 (B. S. Safonov et al. 2017). All other observations from this instrument used a Hamamatsu ORCA-quest CMOS detector (I. A. Strakhov et al. 2023). See Table 5 for a summary of each observation including the dates each system was observed, filters used, contrast achieved, and whether a nearby companion was detected.

Our high-resolution imaging runs resulted in the detection of only two nearby companions, one in the TOI-4462 system and another in the TOI-5240 system (see Figure 1). The companion to TOI-5240 was detected only by PHARO and is 2$''$.4 away at a position angle of 156°. It is 6.67 mag dimmer in the Brγ filter, contributing only 0.1% of the total flux of the unresolved system. Even if this companion is a perfectly edge-on, equal-mass eclipsing binary, the eclipse depths would be an order of magnitude smaller than the observed transit depths. Since it contributes a negligible amount of light to the overall flux of the system, we chose to neglect this companion in our analysis (e.g., M. Mugrauer & K.-U. Michel 2020, 2021).

The companion to TOI-4462 A was resolved by both SAI and PHARO at 0$''$.4 separation and a position angle of 225°. It is approximately 2.6 mag dimmer in the $H_{\rm cont}$ and $K_{\rm cont}$ filters, too bright to neglect in our analysis (see Section 3). However, we remain confident that the Keplerian signals detected in both our photometry and spectroscopy can only be attributed to the brighter primary star. The transits observed by TESS KeplerCam and LCO-TEID show no evidence of chromaticity, and the spectral line profiles show no evidence of a secondary set of spectral lines that would produce an apparent RV shift. Since TRES observed TOI-4462 with a 2$''$.3 fiber (larger than the companion's separation), the host-star spectra were blended with light from the companion. However, this faint companion would only affect the measured RVs at the tens of meters per second level (L. A. Buchhave et al. 2011), significantly smaller than the 10,000 m s^{-1} semi-amplitude we measure for the TOI-4462 system. Hence, we are confident that the signal we detect is due to an unresolved transiting companion around the brighter primary star TOI-4462 A.

3. Analysis

We analyzed each system using `EXOFASTv2` (J. D. Eastman et al. 2019),[41] a publicly available exoplanet fitting suite. `EXOFASTv2` is a differential evolution Markov Chain Monte Carlo (MCMC) code which globally fits both the star and the companion simultaneously, ensuring a self-consistent set of parameters for the entire system. In each fit, we generate a SED model for the host star using MESA Isochrones and Stellar Tracks (MIST; B. Paxton et al. 2011, 2013) in order to fit the host star, while the companion is fit with a standard Keplerian model. Our SED model is fit to broadband archival photometry, which we collected from Gaia Data Release 3 (DR3; Gaia Collaboration et al. 2023), the Two Micron All

---

[41] https://github.com/jdeast/EXOFASTv2

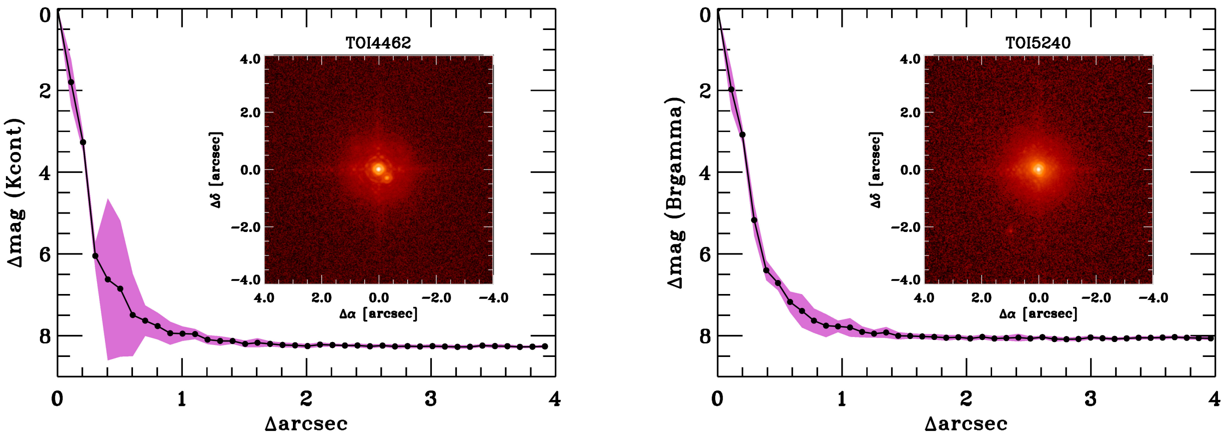

Figure 1. The AO images and contrast curves for TOI-4462 and TOI-5240 taken by PHARO on the 5.0 m Palomar telescope. Left: TOI-4462 in the $K_{\rm cont}$ filter with a bright companion clearly seen at a separation of 0.″4. Right: TOI-5240 in the Brγ filter with a faint companion at a separation of 2.″4.

Table 5
Summary of High-resolution Imaging Observations

Target	Telescope	Instrument	Image Type	Filter	Contrast	Observation Date (UT)	Detection?[a]
TOI-2844	SOAR (4.1 m)	HRCam	Speckle	I_c	Δ 5.8 mag at 1″	2022 Apr 15	No
⋯	WIYN (3.5 m)	NESSI	Speckle	832 nm	⋯	2022 Apr 18	No
TOI-3122	SOAR (4.1 m)	HRCam	Speckle	I_c	Δ 5.0 mag at 1″	2022 Apr 25	No
TOI-3577	Palomar (5.0 m)	PHARO	AO	Brγ	Δ 5.8 mag at 0.″5	2023 Jun 7	No
TOI-3755	SAI (2.5 m)	Speckle Polarimeter	Speckle	I_c	Δ 5.7 mag at 1″	2021 Oct 29	No
TOI-4462	SAI (2.5 m)	Speckle Polarimeter	Speckle	I_c	Δ 6.3 mag at 1″	2023 Jan 22	Yes
⋯	SAI (2.5 m)	Speckle Polarimeter	Speckle	I_c	Δ 5.3 mag at 1″	2024 Feb 24	Yes
⋯	Palomar (5.0 m)	PHARO	AO	$H_{\rm cont}$	Δ 7.2 mag at 0.″5	2024 Apr 21	Yes
⋯	Palomar (5.0 m)	PHARO	AO	$K_{\rm cont}$	Δ 6.9 mag at 0.″5	2024 Apr 21	Yes
TOI-4635	Shane (3.0 m)	ShARCS	AO	J	⋯	2021 Nov 21	No
⋯	Shane (3.0 m)	ShARCS	AO	Ks	⋯	2021 Nov 21	No
⋯	SOAR (4.1 m)	HRCam	Speckle	I_c	Δ 6.7 mag at 1″	2024 Jan 8	No
TOI-4737	Gemini (8.0 m)	Zorro	Speckle	562 nm	Δ 4.3 mag at 0.″5	2022 Mar 19	No
⋯	Gemini (8.0 m)	Zorro	Speckle	832 nm	Δ 6.0 mag at 0.″5	2022 Mar 19	No
⋯	SOAR (4.1 m)	HRCam	Speckle	I_c	Δ 5.6 mag at 1″	2022 Apr 15	No
TOI-4759	SOAR (4.1 m)	HRCam	Speckle	I_c	Δ 6.2 mag at 1″	2022 Apr 15	No
TOI-5240	Palomar (5.0 m)	PHARO	AO	Brγ	Δ 6.7 mag at 0.″5	2023 Jun 6	Yes
⋯	SAI (2.5 m)	Speckle Polarimeter	Speckle	I_c	Δ 6.3 mag at 1″	2023 Sep 1	No
TOI-5467	SAI (2.5 m)	Speckle Polarimeter	Speckle	I_c	Δ 6.2 mag at 1″	2022 Dec 12	No
TOI-5882	Palomar (5.0 m)	PHARO	AO	Brγ	Δ 6.8 mag at 0.″5	2023 Jun 6	No
⋯	SAI (2.5 m)	Speckle Polarimeter	Speckle	I_c	Δ 7.4 mag at 1″	2023 Aug 28	No

Notes. All images and contrast curves are available on ExoFOP.

[a] Detection refers to a positive detection of a star within the field of view of the AO or speckle instrument, subject to the maximum contrast possible with the instrument in question.

Sky Survey (2MASS; R. M. Cutri et al. 2003; M. F. Skrutskie et al. 2006), and the Wide-field Infrared Survey Explorer (WISE; E. L. Wright et al. 2010; R. M. Cutri et al. 2012). The Keplerian model for the companion is fit to the TESS and ground-based transits as well as the RV data from TRES and SOPHIE. For a more detailed explanation of the modeling process, see J. D. Eastman et al. (2019).

The fit was generally set up in the same way for each system, except for TOI-4462, which required special consideration due to the presence of a bright nearby companion, which we discuss in Section 3.1. For the other 11 systems, we first compiled the archival photometry for each target in the Gaia G, Bp, Rp, 2MASS J, H, Ks, and WISE W1, W2, and W3 bands to construct the SED. We then placed a set of priors on each system based on previous observations, the first of which was a Gaussian prior on the parallax from Gaia DR3 with the L. Lindegren et al. (2021) correction applied. The parallax uncertainty was added in quadrature with 0.01 to account for any remaining systematic residuals. We also placed a Gaussian prior on the host-star metallicity centered on the average value of the TRES-derived metallicity with a prior width of twice the standard deviation. Additionally, we place an upper limit on the V-band extinction along the line of sight using the dust maps from D. J. Schlegel et al. (1998) and E. F. Schlafly & D. P. Finkbeiner (2011).

In addition to the priors described above, we also fit for a dilution term in each system to account for unresolved contaminants.To do this, we placed a prior of 0% ± 10% of the contamination ratio reported by the TESS Input Catalog (TIC; K. G. Stassun et al. 2018, 2019). While the QLP and SPOC light curves are both already corrected for known contaminants, we still chose to fit for a dilution term as a conservative assumption that the correction applied had a precision of at most 10%. We did this because the contamination ratio reported by the TIC is only an estimate that does not account for the actual point-spread functions, as the CCD location and camera were unknown until after the launch of TESS. We also provided each fit with starting points on several parameters from the TIC. Specifically, we adopted the TIC-derived values for the host star's mass, radius, and effective temperature as well as the companion's orbital period, time of conjunction, and radius. We retrieved these values from the TESS mission catalog on ExoFOP (NExScI 2022).[42] We performed a preliminary fit with `EXOFASTv2` on each system, which included fitting a linear term to the RVs in order to account for a long-term drift due to unseen outer companions. In every case except for TOI-4737, this resulted in a slope consistent with zero within 1σ, and we subsequently fixed the slope to zero in all subsequent fits for these systems. For TOI-4737, we continued to fit for this long-term trend, and in the final iteration of these fits which we publish here, we found a slope of -1.63 ± 0.23 m s^{-1} day^{-1}. Each system's final fit was run to the adopted convergence criteria suggested by J. D. Eastman et al. (2019) of at least 1000 independent draws and a Gelman–Rubin statistic $<$1.01. See Table 6 for the priors used, and the median values determined from our analysis.

Four of our fits resulted in bimodal posterior distributions. This typically arises when `EXOFASTv2` is unable to distinguish between a host star that is at the end of the main sequence versus the subgiant branch, resulting in high and low stellar mass solutions. Indeed, this was the case in all four bimodal systems presented here (TOI-3577, TOI-4462, TOI-4759, and TOI-5882). We characterized each solution independently by splitting the posterior distributions at the local minimum between the two solutions. We present both solutions for the sake of transparency, but in each case we adopt the higher-probability solution as the preferred parameter set. See Table 7 for the priors used, and the median values determined for both solutions of these bimodal systems. Plots of the transit photometry, RVs, SEDs, and MIST evolutionary tracks for each system presented in this work are presented in Figures 2–12.

3.1. Multi-star Fitting in `EXOFASTv2`

As discussed in Section 2.4, a stellar companion to TOI-4462 was detected $0\rlap{.}''4$ away, which was blended in all catalog photometry and a significant factor in the dilution of the transit light curves. Given that the probability of a chance alignment is low, and the high Gaia renormalized unit weight error of 3.13, we assumed this companion is bound to the primary star. We undid the deblending that SPOC applies to the TESS light curves so that we could more accurately model it based on our multicomponent SED model. We modeled both stars simultaneously, each with its own MIST evolutionary model, while assuming that the age, initial metallicity, distance, and extinction are the same for both stars. In addition, we modeled a SED for each star, constraining the sum of both stars with the catalog photometry of the unresolved TOI-4462 system, and the difference between the two stars with the AO photometry from PHARO, as shown in Figure 1 (left). We therefore fit for dilution terms that were then constrained by the multicomponent SED model, integrated at the transit-observed bands assuming a 5% floor in the theoretical dilution from the model atmospheres. That is, we applied an adaptive prior penalty of

$$\ln \mathscr{L} = 0.5\left(\frac{D_{\rm Step} - D_{\rm SED}}{0.02 D_{\rm Step}}\right)^2, \quad (1)$$

where $D_{\rm Step}$ is the modeled dilution at the current MCMC step, and $D_{\rm SED}$ is the SED-derived dilution. This naturally propagates the uncertainty in the stellar properties, accounting for systematics in the theoretical atmospheres, to the light-curve deblending and transit depth.

4. Discussion

The five BD-mass companions presented here increase the population of transiting brown dwarfs to over 50. While this number is expected to continue growing, it is worth analyzing the sizable population that has been put together thus far in the context of planet-like and star-like formation. We have also added six new transiting low-mass stars to the population $>80\,M_{\rm J}$. Accurate mass and radius measurements are rare for these objects, which will be vital for anchoring our understanding of stellar formation and evolution. We may find that early trends or features observed in the growing population from previous efforts have been reinforced, or lost significance (perhaps even disappearing) in the wake of new discoveries. One such feature of particular interest is the so-called brown dwarf desert and its potential role in dividing the brown dwarfs into distinct planet-like and star-like groups. We discuss these trends below in Sections 4.1 and 4.2. We also note that one of the BD-hosting stars presented here, TOI-5882, has a significant absorption feature at 6708 Å, which we attribute to Li. We discuss in Section 4.3 the implications of this, as well as how it affects our determination of the system's age.

4.1. The Transiting Brown Dwarf Desert

Perhaps the most discussed feature to emerge from the growing transiting BD population is that of the BD desert. The phrase was originally coined in the earliest days of exoplanet discovery (G. W. Marcy et al. 1997; D. W. Latham et al. 1998) in reference to the lack of BD-mass companions discovered by RV surveys at that time. It has since evolved over time with studies like D. Grether & C. H. Lineweaver (2006), which analyzed RV-detected companions with periods less than 5 yr and found the "driest" part of the desert was between 13 and 56 $M_{\rm J}$. Then, B. Ma & J. Ge (2014) examined trends in the RV-discovered population and refined the measurement to be between $35 < m \sin i < 55\,M_{\rm J}$ and with periods less than 100 days.

We now have a more substantial population of transiting BD systems that have precisely measured radii and masses. It is worth exploring how well the trends found in the the RV-discovered sample hold up in the transiting BD regime. Of course, because of the transit probability decreases with period, transiting systems tend to have much shorter orbital periods than their counterparts discovered through direct imaging and RV campaigns. As a result we are largely investigating a different, more limited parameter space than the previous studies of B. Ma & J. Ge (2014), for example. We

---

[42] https://exofop.ipac.caltech.edu/tess/

Table 6
Median Values and 68% Confidence Intervals for Fitted Stellar and Planetary Parameters

		TOI-2844	TOI-3122	TOI-3755	TOI-4635
Priors					
π	Gaia parallax (mas)	$\mathcal{G}[1.4759, 0.01696]$	$\mathcal{G}[1.962, 0.01778]$	$\mathcal{G}[3.0924, 0.01443]$	$\mathcal{G}[13.33, 0.02582]$
[Fe/H]	Metallicity (dex)	$\mathcal{G}[0.025, 0.198]$	$\mathcal{G}[0.3193, 0.1188]$	$\mathcal{G}[0.3156, 0.1007]$	$\mathcal{G}[-0.1783, 0.1608]$
A_V	V-band extinction (mag)	$\mathcal{U}[0, 0.2725]$	$\mathcal{U}[0, 0.4675]$	$\mathcal{U}[0, 0.9867]$	$\mathcal{U}[0, 0.3959]$
D_T	Dilution in TESS	$\mathcal{G}[0, 0.008335]$	$\mathcal{G}[0, 0.027729]$	$\mathcal{G}[0, 0.012054]$	$\mathcal{G}[0, 0.002608]$
Primary Star Parameters					
M_*	Mass ($M_\odot$)	$1.585^{+0.071}_{-0.072}$	$1.247^{+0.074}_{-0.091}$	$1.037^{+0.066}_{-0.071}$	$0.698^{+0.027}_{-0.025}$
R_*	Radius ($R_\odot$)	$1.784^{+0.085}_{-0.08}$	$1.336^{+0.062}_{-0.045}$	$1.044^{+0.042}_{-0.038}$	0.683 ± 0.011
L_*	Luminosity ($L_\odot$)	$6.51^{+0.57}_{-0.48}$	$2.27^{+0.24}_{-0.27}$	$0.99^{+0.12}_{-0.11}$	$0.182^{+0.011}_{-0.013}$
ρ_*	Density (cgs)	$0.394^{+0.065}_{-0.059}$	$0.742^{+0.09}_{-0.12}$	$1.29^{+0.18}_{-0.17}$	3.09 ± 0.12
$\log g$	Surface gravity (cgs)	$4.135^{+0.048}_{-0.051}$	$4.284^{+0.038}_{-0.059}$	$4.417^{+0.043}_{-0.049}$	4.613 ± 0.013
$T_{\rm eff}$	Effective temperature (K)	6910.0 ± 210	6120.0^{+180}_{-220}	5630.0 ± 170	4555.0^{+67}_{-74}
[Fe/H]	Metallicity (dex)	$0.06^{+0.12}_{-0.089}$	0.29 ± 0.11	$0.334^{+0.092}_{-0.098}$	$-0.091^{+0.039}_{-0.033}$
$[\mathrm{Fe/H}]_0$	Initial metallicity	$0.22^{+0.1}_{-0.088}$	$0.298^{+0.094}_{-0.093}$	$0.317^{+0.085}_{-0.093}$	$-0.077^{+0.055}_{-0.051}$
Age	Age (Gyr)	$1.08^{+0.52}_{-0.42}$	$2.5^{+2.6}_{-1.6}$	$4.9^{+4.9}_{-3.5}$	$7.5^{+4.2}_{-4.5}$
EEP	Equal evolutionary phase	$342.5^{+9.5}_{-14}$	351.0^{+59}_{-32}	362.0^{+44}_{-40}	332.0^{+11}_{-24}
A_V	V-band extinction (mag)	$0.132^{+0.084}_{-0.082}$	$0.3^{+0.12}_{-0.17}$	$0.5^{+0.15}_{-0.16}$	$0.26^{+0.1}_{-0.15}$
d	Distance (pc)	$677.0^{+7.9}_{-7.6}$	510.0 ± 4.6	323.5 ± 1.5	$75.01^{+0.15}_{-0.14}$
Companion Parameters					
P	Period (days)	3.5524204 ± 0.000003	6.1836025 ± 0.0000063	$5.543744^{+0.0000062}_{-0.0000061}$	12.2769349 ± 0.0000033
R_P	Radius ($R_{\rm J}$)	$0.775^{+0.047}_{-0.043}$	$1.235^{+0.075}_{-0.057}$	$0.885^{+0.051}_{-0.046}$	1.02 ± 0.019
M_P	Mass ($M_{\rm J}$)	$54.0^{+4.9}_{-5.1}$	$101.5^{+4.1}_{-4.8}$	$47.1^{+2}_{-2.1}$	$84.0^{+2.1}_{-2}$
T_C	Time of conjunction ($\mathrm{BJD_{TDB}}$)	$2459574.31396^{+0.00094}_{-0.00099}$	$2459356.52122^{+0.00067}_{-0.00065}$	$2459914.24483^{+0.00057}_{-0.00058}$	$2459448.74844 \pm 0.00018$
T_0	Optimal conjunction time ($\mathrm{BJD_{TDB}}$)	$2459940.21326^{+0.00088}_{-0.00093}$	$2459727.53737^{+0.00054}_{-0.00052}$	$2459775.65123^{+0.00054}_{-0.00057}$	2460013.48744 ± 0.0001
a	Semimajor axis (au)	$0.0537^{+0.00079}_{-0.00082}$	$0.0728^{+0.0014}_{-0.0018}$	$0.0629^{+0.0013}_{-0.0015}$	$0.0958^{+0.0012}_{-0.0011}$
i	Inclination (degrees)	$83.7^{+2}_{-1.3}$	$87.3^{+1.6}_{-1.5}$	$87.51^{+0.35}_{-0.36}$	$88.791^{+0.057}_{-0.056}$
e	Eccentricity	$0.424^{+0.046}_{-0.041}$	$0.4704^{+0.008}_{-0.0077}$	$0.0049^{+0.0031}_{-0.0026}$	0.4906 ± 0.0015
ω_*	Argument of periastron (degrees)	159.0 ± 11	$75.55^{+0.98}_{-0.91}$	21.0^{+44}_{-57}	$-5.99^{+0.78}_{-0.74}$
$T_{\rm eq}$	Equilibrium temperature (K)	1919.0^{+37}_{-33}	1267.0^{+27}_{-32}	1106.0 ± 28	$586.6^{+8.2}_{-9.5}$
$\tau_{\rm circ}$	Tidal circularization timescale (Gyr)	27.0^{+17}_{-12}	$33.0^{+10}_{-9.7}$	500.0^{+170}_{-130}	827.0^{+71}_{-65}
K	RV semi-amplitude (m $\mathrm{s^{-1}}$)	5700.0^{+450}_{-470}	10450.0 ± 110	5127.0 ± 22	10032.0^{+41}_{-43}
R_P/R_*	Radius of planet in stellar radii	0.0447 ± 0.0013	$0.0952^{+0.0026}_{-0.0025}$	0.0872 ± 0.0025	$0.15339^{+0.00081}_{-0.00082}$
a/R_*	Semimajor axis in stellar radii	6.47 ± 0.34	$11.74^{+0.45}_{-0.68}$	$12.96^{+0.57}_{-0.61}$	30.17 ± 0.38
Depth	TESS flux decrement at mid-transit	0.00212 ± 0.00011	$0.01026^{+0.00056}_{-0.00055}$	0.0085 ± 0.00046	$0.02871^{+0.00036}_{-0.00035}$
τ	Ingress/egress transit duration (days)	$0.0073^{+0.0016}_{-0.0015}$	$0.01015^{+0.0015}_{-0.00082}$	$0.0144^{+0.0017}_{-0.0014}$	0.02135 ± 0.00058
T_{14}	Total transit duration (days)	$0.1258^{+0.0019}_{-0.0018}$	$0.1075^{+0.0019}_{-0.0016}$	$0.1267^{+0.0021}_{-0.0019}$	$0.12316^{+0.00051}_{-0.0005}$
b	Transit impact parameter	$0.52^{+0.11}_{-0.19}$	$0.3^{+0.14}_{-0.17}$	$0.564^{+0.052}_{-0.058}$	$0.509^{+0.017}_{-0.019}$
ρ_P	Density (cgs)	143.0^{+31}_{-27}	67.0^{+10}_{-12}	84.0^{+16}_{-14}	$98.3^{+4.9}_{-4.6}$
$\log g_P$	Surface gravity	$5.346^{+0.065}_{-0.069}$	$5.218^{+0.044}_{-0.062}$	$5.173^{+0.052}_{-0.055}$	5.302 ± 0.014
Θ	Safronov number	$4.71^{+0.49}_{-0.48}$	$9.58^{+0.47}_{-0.54}$	$6.45^{+0.36}_{-0.35}$	$22.57^{+0.47}_{-0.46}$
T_S	Time of eclipse ($\mathrm{BJD_{TDB}}$)	$2459575.217^{+0.086}_{-0.084}$	$2459353.947^{+0.033}_{-0.034}$	$2459911.4849^{+0.0084}_{-0.0091}$	$2459446.27^{+0.011}_{-0.01}$
$T_{S,14}$	Total eclipse duration (days)	$0.142^{+0.035}_{-0.011}$	$0.205^{+0.069}_{-0.2}$	$0.1269^{+0.0021}_{-0.002}$	0.1137 ± 0.0013
$e \cos \omega_*$		$-0.391^{+0.042}_{-0.04}$	$0.1173^{+0.0076}_{-0.0078}$	$0.0034^{+0.0024}_{-0.0026}$	0.4878 ± 0.0016
$e \sin \omega_*$		$0.148^{+0.088}_{-0.078}$	$0.4555^{+0.0082}_{-0.0078}$	$0.001^{+0.0039}_{-0.0032}$	$-0.0511^{+0.0066}_{-0.0063}$
M_P/M_*	Mass ratio	$0.0326^{+0.0028}_{-0.003}$	$0.0778^{+0.0023}_{-0.0018}$	$0.04337^{+0.0011}_{-0.00093}$	0.1148 ± 0.0016
d/R_*	Separation at mid-transit	$4.62^{+0.56}_{-0.58}$	$6.26^{+0.28}_{-0.36}$	$12.95^{+0.58}_{-0.6}$	24.14 ± 0.41

		TOI-4737	TOI-5240	TOI-5467
Priors				
π	Gaia parallax (mas)	$\mathcal{G}[1.7399, 0.01656]$	$\mathcal{G}[1.0355, 0.01516]$	$\mathcal{G}[1.7819, 0.01704]$
[Fe/H]	Metallicity (dex)	$\mathcal{G}[0.3267, 0.1499]$	$\mathcal{G}[-0.1571, 0.2089]$	$\mathcal{G}[0.3257, 0.1645]$
A_V	V-band extinction (mag)	$\mathcal{U}[0, 1.8386]$	$\mathcal{U}[0, 0.4879]$	$\mathcal{U}[0, 1.6687]$
D_T	Dilution in TESS	$\mathcal{G}[0, 0.005883]$	$\mathcal{G}[0, 0.024878]$	$\mathcal{G}[0, 0.007941]$

Table 6
(Continued)

		TOI-4737	TOI-5240	TOI-5467
Primary Star Parameters				
M_*	Mass ($M_\odot$)	$1.336^{+0.08}_{-0.09}$	$1.754^{+0.094}_{-0.092}$	$1.515^{+0.059}_{-0.058}$
R_*	Radius ($R_\odot$)	$1.618^{+0.068}_{-0.066}$	2.35 ± 0.11	$1.503^{+0.046}_{-0.045}$
L_*	Luminosity ($L_\odot$)	$3.39^{+0.34}_{-0.31}$	$14.9^{+2.4}_{-2.1}$	$4.4^{+0.41}_{-0.33}$
ρ_*	Density (cgs)	$0.443^{+0.073}_{-0.065}$	$0.189^{+0.032}_{-0.026}$	$0.63^{+0.054}_{-0.052}$
$\log g$	Surface gravity (cgs)	$4.145^{+0.05}_{-0.053}$	$3.938^{+0.049}_{-0.047}$	$4.266^{+0.024}_{-0.027}$
$T_{\rm eff}$	Effective temperature (K)	6160.0^{+210}_{-200}	7390.0^{+350}_{-330}	6820.0^{+170}_{-150}
[Fe/H]	Metallicity (dex)	$0.24^{+0.1}_{-0.11}$	-0.12 ± 0.19	$0.265^{+0.098}_{-0.11}$
$[{\rm Fe/H}]_0$	Initial metallicity	$0.297^{+0.093}_{-0.096}$	$-0.03^{+0.18}_{-0.19}$	$0.316^{+0.083}_{-0.093}$
Age	Age (Gyr)	$3.0^{+1.6}_{-1.3}$	$1.19^{+0.23}_{-0.2}$	$0.29^{+0.42}_{-0.2}$
EEP	Equal evolutionary phase	377.0^{+38}_{-32}	374.0^{+13}_{-14}	294.0^{+27}_{-37}
A_V	V-band extinction (mag)	0.4 ± 0.11	$0.23^{+0.15}_{-0.14}$	$0.567^{+0.092}_{-0.08}$
d	Distance (pc)	$574.5^{+5.5}_{-5.4}$	966.0 ± 14	$560.5^{+5.4}_{-5.2}$
Companion Parameters				
P	Period (days)	$9.320278^{+0.000018}_{-0.000017}$	4.1793241 ± 0.0000058	$2.6570963^{+0.0000027}_{-0.0000028}$
R_P	Radius ($R_{\rm J}$)	$0.701^{+0.079}_{-0.059}$	$1.655^{+0.097}_{-0.096}$	$1.096^{+0.046}_{-0.043}$
M_P	Mass ($M_{\rm J}$)	$66.3^{+2.7}_{-3.1}$	$128.0^{+4.9}_{-4.8}$	$91.7^{+2.8}_{-2.7}$
T_C	Time of conjunction ($\rm BJD_{TDB}$)	$2459222.4062^{+0.0017}_{-0.0018}$	$2459444.90408^{+0.0009}_{-0.00091}$	$2459545.35471^{+0.00052}_{-0.00053}$
T_0	Optimal conjunction time ($\rm BJD_{TDB}$)	2459949.3884 ± 0.0011	$2459950.60229 \pm 0.00057$	$2459927.97657 \pm 0.00035$
a	Semimajor axis (au)	$0.097^{+0.0019}_{-0.0022}$	0.0626 ± 0.0011	$0.04394^{+0.00056}_{-0.00055}$
i	Inclination (degrees)	$87.82^{+0.51}_{-0.46}$	$85.7^{+1.4}_{-1.1}$	$83.21^{+0.35}_{-0.37}$
e	Eccentricity	$0.0063^{+0.007}_{-0.0042}$	$0.0113^{+0.014}_{-0.0078}$	$0.0137^{+0.013}_{-0.0083}$
ω_*	Argument of periastron (degrees)	-120.0^{+40}_{-89}	-115.0^{+28}_{-83}	121.0^{+57}_{-28}
$T_{\rm eq}$	Equilibrium temperature (K)	1214.0^{+26}_{-25}	2187.0^{+80}_{-81}	1924.0^{+39}_{-34}
$\tau_{\rm circ}$	Tidal circularization timescale (Gyr)	$25000.0^{+15000}_{-11000}$	$25.7^{+9.5}_{-6.6}$	$18.1^{+3.8}_{-3.3}$
K	RV semi-amplitude (m s^{-1})	5118.0 ± 49	10580.0^{+160}_{-150}	9760.0^{+130}_{-140}
R_P/R_*	Radius of planet in stellar radii	$0.0443^{+0.0047}_{-0.003}$	0.0723 ± 0.0019	0.075 ± 0.0017
a/R_*	Semimajor axis in stellar radii	$12.86^{+0.67}_{-0.66}$	$5.72^{+0.31}_{-0.27}$	$6.29^{+0.17}_{-0.18}$
Depth	TESS flux decrement at mid-transit	$0.00216^{+0.00048}_{-0.00028}$	0.00563 ± 0.0003	0.00569 ± 0.00025
τ	Ingress/egress transit duration (days)	$0.012^{+0.0019}_{-0.0015}$	$0.0192^{+0.0023}_{-0.0022}$	$0.015^{+0.0011}_{-0.001}$
T_{14}	Total transit duration (days)	$0.214^{+0.0029}_{-0.0027}$	$0.232^{+0.0023}_{-0.0022}$	0.1053 ± 0.0012
b	Transit impact parameter	$0.491^{+0.074}_{-0.095}$	$0.436^{+0.084}_{-0.13}$	$0.735^{+0.018}_{-0.02}$
ρ_P	Density (cgs)	236.0^{+76}_{-67}	$35.0^{+7.2}_{-5.7}$	$86.5^{+11}_{-9.8}$
$\log g_P$	Surface gravity	$5.521^{+0.083}_{-0.098}$	$5.063^{+0.056}_{-0.053}$	$5.278^{+0.034}_{-0.035}$
Θ	Safronov number	$13.7^{+1.3}_{-1.4}$	$5.52^{+0.34}_{-0.31}$	$4.85^{+0.22}_{-0.21}$
T_S	Time of eclipse ($\rm BJD_{TDB}$)	$2459227.054^{+0.016}_{-0.022}$	$2459446.983^{+0.012}_{-0.014}$	$2459546.6736^{+0.0091}_{-0.011}$
$T_{S,14}$	Total eclipse duration (days)	$0.213^{+0.0035}_{-0.0036}$	$0.2294^{+0.0042}_{-0.006}$	0.1054 ± 0.0011
$e\cos\omega_*$		$-0.002^{+0.0027}_{-0.0037}$	$-0.0039^{+0.0043}_{-0.0053}$	$-0.0057^{+0.0054}_{-0.0067}$
$e\sin\omega_*$		$-0.0026^{+0.0046}_{-0.0089}$	$-0.0065^{+0.0084}_{-0.017}$	$0.009^{+0.015}_{-0.0093}$
M_P/M_*	Mass ratio	$0.0474^{+0.0013}_{-0.0011}$	$0.0696^{+0.0018}_{-0.0017}$	0.0578 ± 0.0012
d/R_*	Separation at mid-transit	$12.92^{+0.68}_{-0.67}$	$5.77^{+0.32}_{-0.29}$	$6.22^{+0.2}_{-0.21}$

Note. The priors listed at the top of the table are labeled as $\mathcal{G}$[mean, standard deviation] if they are Gaussian priors and $\mathcal{U}$[lower limit, upper limit] if they are uniform priors.

found that the most sparsely populated area of the transiting BD desert appears to be the entire low-mass BD regime ($<\sim 42\,M_{\rm J}$), and the work presented here contributes one new BD (TOI-5882) to this underpopulated region (see Figure 13). We also note that the apparent drop-off in systems with companions above the substellar limit ($80\,M_{\rm J}$) is likely unphysical, and is more plausibly due to selection bias since most of these systems have been discovered via exoplanet discovery pipelines. In order to more accurately describe trends emerging near the hydrogen fusion boundary, a more unbiased sample will need to be produced.

Another key trend that was first noted by the B. Ma & J. Ge (2014) RV study is in the eccentricity versus $m \sin i$ distribution. They found that eccentricity decreases as

Table 7

Median Values and 68% Confidence Intervals for Fitted Stellar and Planetary Parameters for Bimodal Systems

		TOI-3577		TOI-4462	
		Low-mass Solution (63.8% Probability)	High-mass Solution (36.2% Probability)	Low-mass Solution (90.7% Probability)	High-mass Solution (9.3% Probability)
Priors					
π	Gaia parallax (mas)	$\mathcal{G}[2.36440, 0.01487]$		$\mathcal{G}[2.53984, 0.03785]$	
[Fe/H]	Metallicity (dex)	$\mathcal{G}[-0.0486, 0.0889]$		$\mathcal{G}[0.0873, 0.1781]$	
A_V	V-band extinction (mag)	$\mathcal{U}[0, 2.2165]$		$\mathcal{U}[0, 0.0949]$	
D_T	Dilution in TESS	$\mathcal{G}[0, 0.032559]$		$\mathcal{G}[0, 0.057591]$	
Primary Star Parameters					
M_*	Mass ($M_\odot$)	$1.111^{+0.057}_{-0.067}$	$1.31^{+0.073}_{-0.056}$	$1.252^{+0.053}_{-0.061}$	$1.452^{+0.049}_{-0.047}$
R_*	Radius ($R_\odot$)	$1.753^{+0.068}_{-0.067}$	$1.733^{+0.069}_{-0.064}$	$2.084^{+0.084}_{-0.059}$	$2.128^{+0.046}_{-0.036}$
L_*	Luminosity ($L_\odot$)	$3.38^{+0.5}_{-0.42}$	$4.06^{+0.59}_{-0.52}$	$4.98^{+0.28}_{-0.24}$	$5.07^{+0.24}_{-0.22}$
ρ_*	Density (cgs)	$0.29^{+0.037}_{-0.034}$	$0.355^{+0.047}_{-0.038}$	$0.195^{+0.017}_{-0.023}$	$0.2132^{+0.0075}_{-0.011}$
$\log g$	Surface gravity (cgs)	$3.995^{+0.038}_{-0.04}$	$4.078^{+0.04}_{-0.034}$	$3.898^{+0.026}_{-0.04}$	$3.945^{+0.011}_{-0.015}$
$T_{\rm eff}$	Effective temperature (K)	5920.0 ± 210	6210.0^{+240}_{-200}	5970.0 ± 110	5930.0^{+84}_{-82}
[Fe/H]	Metallicity (dex)	$-0.031^{+0.071}_{-0.069}$	$-0.026^{+0.081}_{-0.073}$	$0.05^{+0.15}_{-0.13}$	$0.19^{+0.13}_{-0.14}$
$[{\rm Fe/H}]_0$	Initial metallicity	$0.021^{+0.066}_{-0.064}$	$0.074^{+0.076}_{-0.068}$	0.09 ± 0.12	$0.22^{+0.11}_{-0.12}$
Age	Age (Gyr)	$6.8^{+1.8}_{-1.3}$	$3.29^{+0.68}_{-0.89}$	$4.73^{+0.75}_{-0.58}$	$2.88^{+0.36}_{-0.33}$
EEP	Equal evolutionary phase	$453.5^{+4.5}_{-7.7}$	398.0^{+15}_{-28}	$454.5^{+3.9}_{-5.4}$	$407.3^{+6.4}_{-7.4}$
A_V	V-band extinction (mag)	$0.31^{+0.16}_{-0.17}$	0.53 ± 0.15	$0.054^{+0.029}_{-0.035}$	$0.063^{+0.023}_{-0.036}$
d	Distance (pc)	423.2 ± 2.7	423.4 ± 2.7	$392.6^{+5.8}_{-5.6}$	$395.2^{+5.7}_{-5.5}$
Companion Parameters					
P	Period (days)	5.266759 ± 0.000013	$5.266759^{+0.000014}_{-0.000013}$	$4.9132987^{+0.0000088}_{-0.0000089}$	$4.9132998^{+0.0000088}_{-0.0000089}$
R_P	Radius ($R_{\rm J}$)	$0.999^{+0.053}_{-0.051}$	$0.967^{+0.053}_{-0.048}$	$1.141^{+0.081}_{-0.078}$	1.158 ± 0.075
M_P	Mass ($M_{\rm J}$)	$53.8^{+1.9}_{-2.2}$	$60.0^{+2.2}_{-1.7}$	$101.7^{+2.8}_{-3.2}$	$111.9^{+2.5}_{-2.4}$
T_C	Time of conjunction (BJD$_{\rm TDB}$)	$2459847.67307^{+0.00091}_{-0.00092}$	$2459847.673^{+0.00093}_{-0.0009}$	$2459789.41867 \pm 0.00079$	$2459789.4187^{+0.00078}_{-0.00079}$
T_0	Optimal conjunction time (BJD$_{\rm TDB}$)	$2460105.74424^{+0.00064}_{-0.00063}$	$2460105.74423^{+0.0006}_{-0.00062}$	$2459882.77168 \pm 0.00077$	$2459882.77175^{+0.00076}_{-0.00077}$
a	Semimajor axis (au)	$0.0623^{+0.001}_{-0.0013}$	$0.06576^{+0.0012}_{-0.00093}$	$0.06251^{+0.00085}_{-0.001}$	$0.06558^{+0.00072}_{-0.0007}$
i	Inclination (degrees)	$83.56^{+0.36}_{-0.38}$	84.14 ± 0.34	$87.7^{+1.4}_{-1.3}$	$89.02^{+0.69}_{-0.97}$
e	Eccentricity	$0.006^{+0.0081}_{-0.0042}$	$0.0066^{+0.0087}_{-0.0047}$	$0.0203^{+0.0034}_{-0.0038}$	$0.0199^{+0.0034}_{-0.004}$
ω_*	Argument of periastron (degrees)	-77.0^{+86}_{-47}	-78.0^{+80}_{-37}	$96.5^{+5.9}_{-5.8}$	$96.5^{+6.1}_{-6}$
$T_{\rm eq}$	Equilibrium temperature (K)	1512.0^{+47}_{-43}	1540.0 ± 47	1663.0^{+27}_{-23}	1630.0^{+20}_{-19}
$\tau_{\rm circ}$	Tidal circularization timescale (Gyr)	258.0^{+80}_{-62}	378.0^{+110}_{-87}	214.0^{+90}_{-63}	241.0^{+95}_{-64}
K	RV semi-amplitude (m s^{-1})	5656.0^{+40}_{-48}	5655.0^{+40}_{-46}	9954.0^{+31}_{-33}	9954.0^{+32}_{-34}
R_P/R_*	Radius of planet in stellar radii	0.0586 ± 0.0012	0.0574 ± 0.0011	$0.0561^{+0.0033}_{-0.0034}$	$0.0558^{+0.0034}_{-0.0035}$
a/R_*	Semimajor axis in stellar radii	7.63 ± 0.31	$8.16^{+0.34}_{-0.31}$	$6.45^{+0.18}_{-0.27}$	$6.635^{+0.077}_{-0.11}$
Depth	TESS flux decrement at mid-transit	0.00317 ± 0.0001	$0.003137^{+0.000099}_{-0.000098}$	$0.00359^{+0.00044}_{-0.00042}$	$0.00361^{+0.00045}_{-0.00044}$
τ	Ingress/egress transit duration (days)	$0.0262^{+0.0028}_{-0.0026}$	$0.0222^{+0.0023}_{-0.0021}$	$0.014^{+0.0015}_{-0.0012}$	$0.01323^{+0.00092}_{-0.00088}$
T_{14}	Total transit duration (days)	$0.1372^{+0.0027}_{-0.0025}$	$0.1339^{+0.0023}_{-0.0022}$	$0.2447^{+0.0024}_{-0.0023}$	$0.2433^{+0.0022}_{-0.0021}$
b	Transit impact parameter	$0.86^{+0.012}_{-0.014}$	$0.838^{+0.015}_{-0.016}$	$0.26^{+0.12}_{-0.15}$	$0.112^{+0.11}_{-0.078}$
ρ_P	Density (cgs)	$66.7^{+12}_{-9.9}$	82.0^{+14}_{-12}	84.0^{+20}_{-16}	89.0^{+20}_{-15}
$\log g_P$	Surface gravity	5.125 ± 0.048	$5.201^{+0.047}_{-0.045}$	$5.286^{+0.061}_{-0.06}$	$5.316^{+0.058}_{-0.054}$
Θ	Safronov number	$6.03^{+0.33}_{-0.3}$	6.21 ± 0.32	$8.89^{+0.65}_{-0.59}$	$8.72^{+0.61}_{-0.53}$
T_S	Time of eclipse (BJD$_{\rm TDB}$)	$2459845.0427^{+0.011}_{-0.0087}$	$2459845.0428^{+0.011}_{-0.0091}$	$2459791.8682^{+0.0062}_{-0.0065}$	$2459791.8684^{+0.0064}_{-0.0065}$
$T_{S,14}$	Total eclipse duration (days)	$0.1381^{+0.0036}_{-0.0031}$	$0.1347^{+0.003}_{-0.0027}$	$0.2539^{+0.0028}_{-0.0029}$	$0.2528^{+0.0029}_{-0.003}$
$e \cos \omega_*$		$0.0009^{+0.0034}_{-0.0026}$	$0.0009^{+0.0034}_{-0.0028}$	$-0.0023^{+0.002}_{-0.0021}$	-0.0022 ± 0.0021
$e \sin \omega_*$		$-0.0031^{+0.0044}_{-0.0097}$	$-0.0041^{+0.005}_{-0.01}$	$0.0201^{+0.0034}_{-0.0038}$	$0.0197^{+0.0034}_{-0.0041}$
M_P/M_*	Mass ratio	$0.04626^{+0.0011}_{-0.00087}$	$0.04365^{+0.00075}_{-0.00091}$	$0.0776^{+0.0014}_{-0.0012}$	0.07359 ± 0.0009
d/R_*	Separation at mid-transit	$7.67^{+0.33}_{-0.32}$	$8.21^{+0.36}_{-0.32}$	$6.32^{+0.18}_{-0.26}$	$6.503^{+0.09}_{-0.12}$

		TOI-4759		TOI-5882	
		Low-mass solution (68.2% probability)	High-mass solution (31.8% probability)	Low-mass solution (71.1% probability)	High-mass solution (28.9% probability)
Priors					
π	Gaia parallax (mas)	$\mathcal{G}[1.34392, 0.01465]$		$\mathcal{G}[2.42207, 0.01753]$	
[Fe/H]	Metallicity (dex)	$\mathcal{G}[0.2723, 0.4141]$		$\mathcal{G}[0.1400, 0.1900]$	
A_V	V-band extinction (mag)	$\mathcal{U}[0, 0.1507]$		$\mathcal{U}[0, 0.8438]$	
D_T	Dilution in TESS	$\mathcal{G}[0, 0.038128]$		$\mathcal{G}[0, 0.008565]$	

Table 7
(Continued)

		TOI-4759		TOI-5882	
		Low-mass solution (68.2% probability)	High-mass solution (31.8% probability)	Low-mass solution (71.1% probability)	High-mass solution (28.9% probability)
Stellar Parameters					
M_*	Mass ($M_\odot$)	$1.186^{+0.061}_{-0.079}$	$1.384^{+0.049}_{-0.048}$	$1.334^{+0.055}_{-0.065}$	$1.549^{+0.055}_{-0.053}$
R_*	Radius ($R_\odot$)	$1.953^{+0.1}_{-0.094}$	$1.868^{+0.083}_{-0.077}$	$2.26^{+0.072}_{-0.052}$	$2.334^{+0.047}_{-0.041}$
L_*	Luminosity ($L_\odot$)	$3.5^{+0.2}_{-0.18}$	$3.49^{+0.15}_{-0.16}$	$5.67^{+0.84}_{-0.73}$	$6.65^{+0.84}_{-0.73}$
ρ_*	Density (cgs)	$0.223^{+0.037}_{-0.034}$	$0.299^{+0.038}_{-0.033}$	$0.1635^{+0.0094}_{-0.015}$	$0.1722^{+0.0065}_{-0.0078}$
$\log g$	Surface gravity (cgs)	$3.928^{+0.047}_{-0.052}$	$4.036^{+0.035}_{-0.033}$	$3.856^{+0.018}_{-0.03}$	$3.892^{+0.012}_{-0.013}$
T_{eff}	Effective temperature (K)	5650.0 ± 150	5770.0 ± 130	5920.0 ± 210	6060.0 ± 180
[Fe/H]	Metallicity (dex)	$0.17^{+0.21}_{-0.22}$	$0.37^{+0.11}_{-0.15}$	$0.18^{+0.16}_{-0.15}$	0.25 ± 0.15
$[\mathrm{Fe/H}]_0$	Initial metallicity	$0.18^{+0.18}_{-0.2}$	$0.376^{+0.088}_{-0.13}$	$0.19^{+0.14}_{-0.13}$	$0.28^{+0.12}_{-0.13}$
Age	Age (Gyr)	$6.25^{+1.1}_{-0.86}$	$3.48^{+0.53}_{-0.54}$	$4.11^{+0.66}_{-0.52}$	$2.44^{+0.34}_{-0.33}$
EEP	Equal evolutionary phase	$457.5^{+5.7}_{-6.2}$	$405.3^{+8.6}_{-14}$	$455.4^{+4.4}_{-5.9}$	$405.5^{+7.2}_{-9.2}$
A_V	V-band extinction (mag)	$0.094^{+0.041}_{-0.057}$	$0.109^{+0.031}_{-0.054}$	$0.33^{+0.17}_{-0.18}$	$0.53^{+0.13}_{-0.14}$
d	Distance (pc)	$743.7^{+8.2}_{-8}$	$743.8^{+8.2}_{-7.9}$	$413.0^{+3}_{-2.9}$	$413.8^{+3}_{-2.9}$
Planetary Parameters					
P	Period (days)	$9.657846^{+0.000036}_{-0.000039}$	$9.657845^{+0.000036}_{-0.000039}$	7.148972 ± 0.000014	7.148973 ± 0.000015
R_P	Radius (R_{J})	$0.926^{+0.069}_{-0.063}$	$0.867^{+0.056}_{-0.052}$	$1.023^{+0.045}_{-0.038}$	$1.056^{+0.037}_{-0.034}$
M_P	Mass (M_{J})	$99.0^{+3.4}_{-4.3}$	$109.4^{+2.6}_{-2.5}$	$22.01^{+0.61}_{-0.72}$	$24.29^{+0.58}_{-0.56}$
T_C	Time of conjunction ($\mathrm{BJD_{TDB}}$)	2459226.0099 ± 0.0035	$2459226.0089^{+0.0035}_{-0.0034}$	$2459818.9045^{+0.0013}_{-0.0012}$	$2459818.9044^{+0.0013}_{-0.0012}$
T_0	Optimal conjunction time ($\mathrm{BJD_{TDB}}$)	$2459370.8776^{+0.0035}_{-0.0034}$	2459370.8766 ± 0.0034	$2459768.8621^{+0.0013}_{-0.0012}$	$2459768.8621^{+0.0013}_{-0.0012}$
a	Semimajor axis (au)	$0.0964^{+0.0016}_{-0.0021}$	$0.1013^{+0.0011}_{-0.0012}$	$0.0804^{+0.0011}_{-0.0013}$	$0.08445^{+0.00099}_{-0.00098}$
i	Inclination (degrees)	$86.97^{+0.58}_{-0.53}$	$87.98^{+0.75}_{-0.53}$	$88.56^{+0.97}_{-1.1}$	$89.25^{+0.52}_{-0.76}$
e	Eccentricity	$0.2411^{+0.0024}_{-0.0026}$	$0.2413^{+0.0024}_{-0.0026}$	0.0339 ± 0.0041	$0.0332^{+0.004}_{-0.0042}$
ω_*	Argument of periastron (degrees)	-19.2 ± 1.5	-19.1 ± 1.5	$104.7^{+4.9}_{-4.5}$	$105.0^{+5.1}_{-4.6}$
T_{eq}	Equilibrium temperature (K)	1226.0^{+24}_{-18}	1194.0 ± 14	1515.0^{+50}_{-46}	1537.0^{+45}_{-43}
τ_{circ}	Tidal circularization timescale (Gyr)	5400.0^{+2400}_{-1700}	9200.0^{+3300}_{-2400}	369.0^{+74}_{-70}	385.0^{+66}_{-57}
K	RV semi-amplitude (m $\mathrm{s^{-1}}$)	8247.0 ± 44	8247.0^{+44}_{-45}	1895.9 ± 7	$1895.9^{+7.2}_{-6.9}$
R_P/R_*	Radius of planet in stellar radii	0.0487 ± 0.0019	0.0477 ± 0.0018	0.0465 ± 0.0013	$0.0465^{+0.0012}_{-0.0013}$
a/R_*	Semimajor axis in stellar radii	$10.59^{+0.55}_{-0.57}$	$11.66^{+0.48}_{-0.45}$	$7.66^{+0.14}_{-0.24}$	$7.786^{+0.097}_{-0.12}$
Depth	TESS flux decrement at mid-transit	0.00263 ± 0.00019	$0.00261^{+0.0002}_{-0.00019}$	0.00251 ± 0.00014	0.0025 ± 0.00014
τ	Ingress/egress transit duration (days)	$0.0183^{+0.0027}_{-0.0022}$	$0.0146^{+0.0017}_{-0.0015}$	$0.01376^{+0.0011}_{-0.00061}$	$0.01337^{+0.00052}_{-0.00044}$
T_{14}	Total transit duration (days)	$0.2698^{+0.0087}_{-0.0083}$	$0.267^{+0.0086}_{-0.0082}$	0.2969 ± 0.0029	0.2951 ± 0.0029
b	Transit impact parameter	$0.573^{+0.069}_{-0.089}$	$0.42^{+0.095}_{-0.15}$	$0.19^{+0.13}_{-0.12}$	$0.098^{+0.097}_{-0.068}$
ρ_P	Density (cgs)	154.0^{+37}_{-30}	208.0^{+42}_{-35}	$25.4^{+2.9}_{-3}$	$25.6^{+2.5}_{-2.4}$
$\log g_P$	Surface gravity	$5.455^{+0.064}_{-0.065}$	5.557 ± 0.053	$4.716^{+0.032}_{-0.036}$	$4.732^{+0.027}_{-0.028}$
Θ	Safronov number	$17.4^{+1.3}_{-1.2}$	$18.5^{+1.2}_{-1.1}$	$2.59^{+0.1}_{-0.11}$	$2.505^{+0.084}_{-0.085}$
T_S	Time of eclipse ($\mathrm{BJD_{TDB}}$)	$2459222.573^{+0.014}_{-0.015}$	$2459222.573^{+0.014}_{-0.015}$	2459822.44 ± 0.012	2459822.44 ± 0.012
$T_{S,14}$	Total eclipse duration (days)	$0.2433^{+0.008}_{-0.0075}$	$0.2339^{+0.0068}_{-0.0065}$	0.3158 ± 0.004	$0.3141^{+0.004}_{-0.0039}$
$e \cos \omega_*$		$0.2277^{+0.0024}_{-0.0026}$	$0.2279^{+0.0025}_{-0.0027}$	-0.0086 ± 0.0026	$-0.0085^{+0.0025}_{-0.0027}$
$e \sin \omega_*$		$-0.0791^{+0.0061}_{-0.0062}$	-0.0791 ± 0.0062	$0.0327^{+0.0041}_{-0.0042}$	$0.032^{+0.0041}_{-0.0043}$
M_P/M_*	Mass ratio	$0.0797^{+0.002}_{-0.0015}$	0.0755 ± 0.001	$0.01574^{+0.00027}_{-0.00022}$	$0.01497^{+0.00018}_{-0.00019}$
d/R_*	Separation at mid-transit	$10.83^{+0.57}_{-0.58}$	$11.92^{+0.5}_{-0.46}$	$7.4^{+0.15}_{-0.23}$	$7.53^{+0.11}_{-0.13}$

companion mass increases up until $m \sin i \sim 42\,M_{\mathrm{J}}$, right in the middle of the driest part of the BD desert. On the other hand, companions more massive than $42\,M_{\mathrm{J}}$ cover a much larger range in eccentricity and have little to no correlation with the companion mass. The authors attributed this trend as evidence of a $\sim 42\,M_{\mathrm{J}}$ transition point between the planet and star formation mechanisms. As the transiting BD population has developed, several studies have drawn comparisons to these results, some finding evidence for the same trends (N. Grieves et al. 2021; B. A. Henderson et al. 2024a), while others have noted low-mass BDs with higher than expected eccentricities (E. Page et al. 2024). However, such claims have historically been subject to the small sample size and selection effects that accompany the transiting BD population. Now that this population exceeds 50 systems, we can at least start to alleviate the risks of small number statistics. Figure 14 (left) shows the eccentricity versus companion mass distribution for the transiting brown dwarfs, and it is clear that there are more systems above $42\,M_{\mathrm{J}}$ with high eccentricity than there are below. About 30% of systems below $42\,M_{\mathrm{J}}$ have eccentricities >0.1 compared to about 45% for

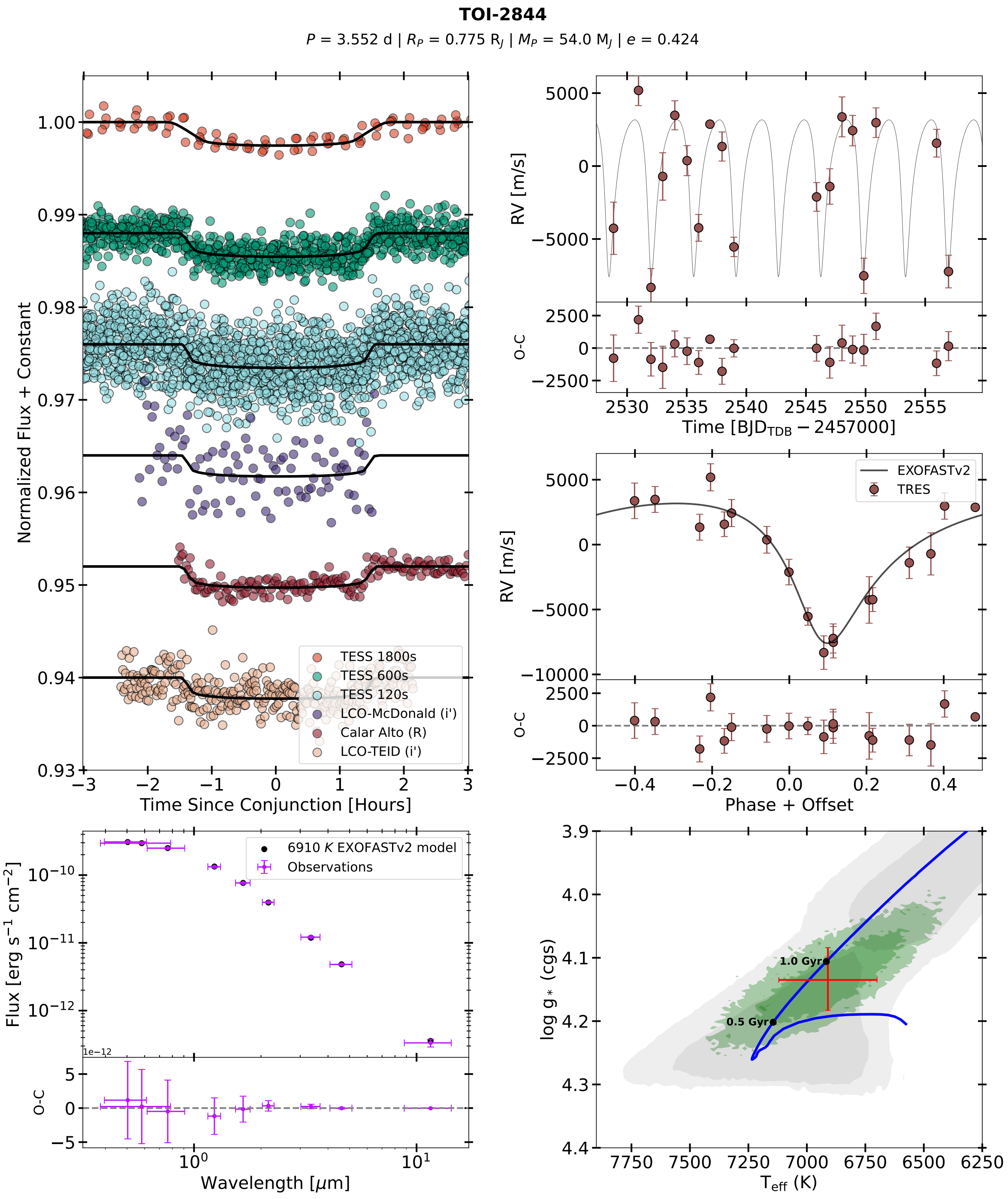

Figure 2. TESS, follow-up, and archival observations of TOI-2844 compared to the the `EXOFASTv2` results. Upper left: unbinned TESS and follow-up ground-based transits, phase-folded and shown in comparison to the best-fit `EXOFASTv2` model with an arbitrary normalized flux offset. Multiple TESS sectors in the same cadence are stacked on top of each other. Bottom left: the SED of the target star compared to the best-fit `EXOFASTv2` model. Residuals are shown on a linear scale, using the same units as the primary y-axis. Upper right: RV observations vs. time, including any significant long-term trend. The residuals are shown in the subpanel below in the same units. Middle right: RV observations phase-folded using the best-fit ephemeris from the `EXOFASTv2` global fit. The phase is shifted so that the transit occurs at phase + offset = 0. The residuals are shown in the subpanel below in the same units. Bottom right: the evolutionary track and current evolutionary stage of the primary star according to the best-fit MIST model. The blue line indicates the best-fit MIST track, while the gray shaded contours show the 1σ and 2σ constraints on the star's current $T_{\rm eff}$ and $\log g$ from the MIST isochrone alone. The green contours represent the 1σ and 2σ constraints on the star's $T_{\rm eff}$ and $\log g$ from the `EXOFASTv2` global fit, combining constraints from observations of the star and planet. The red cross indicates the median and 68% confidence interval.

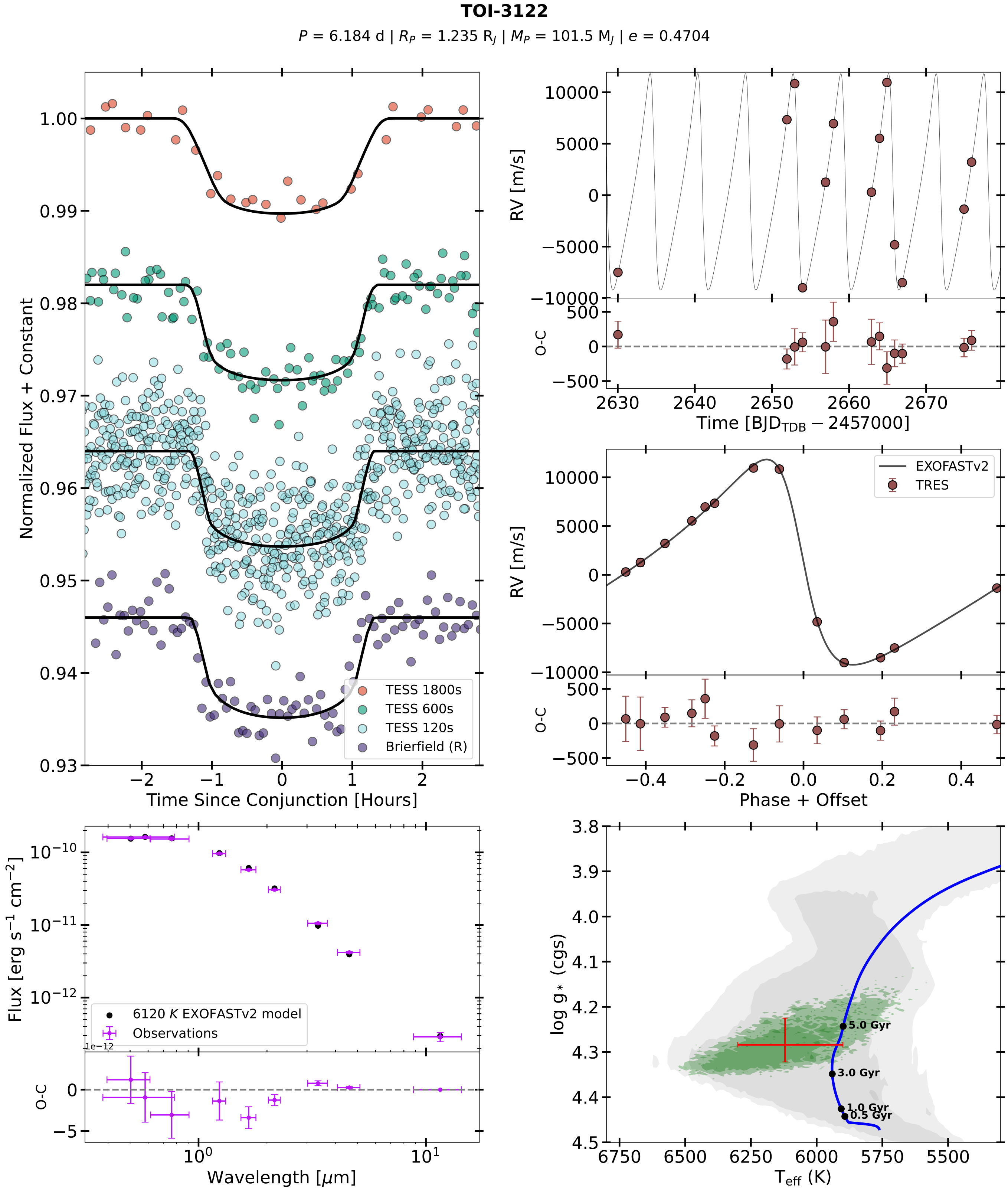

Figure 3. Same as Figure 2 except for TOI-3122.

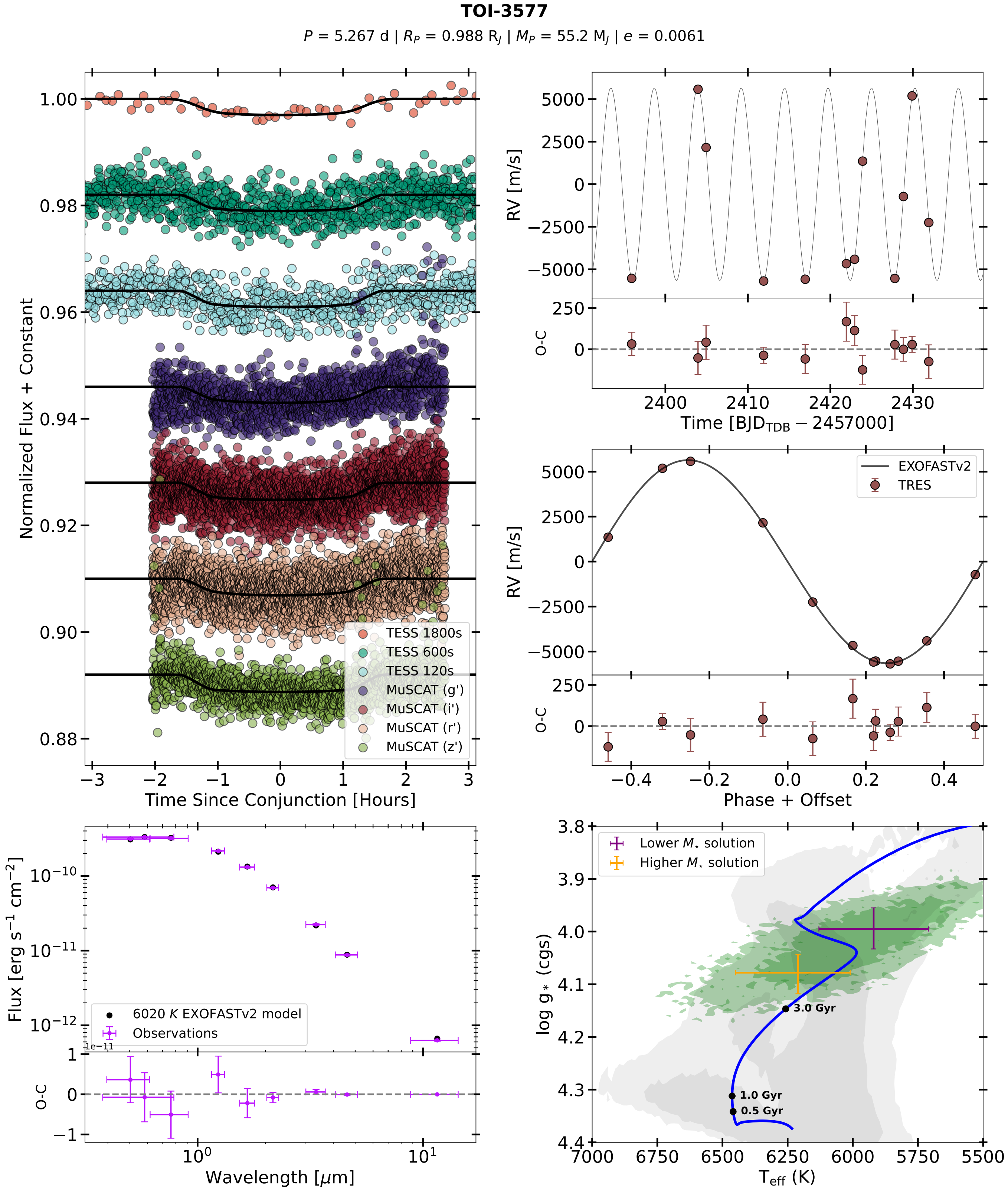

Figure 4. Same as Figure 2 except for TOI-3577. TOI-3577's fit resulted in a bimodal solution. We characterized both solutions independently as described in Section 3, and they are both are shown in the bottom-right plot.

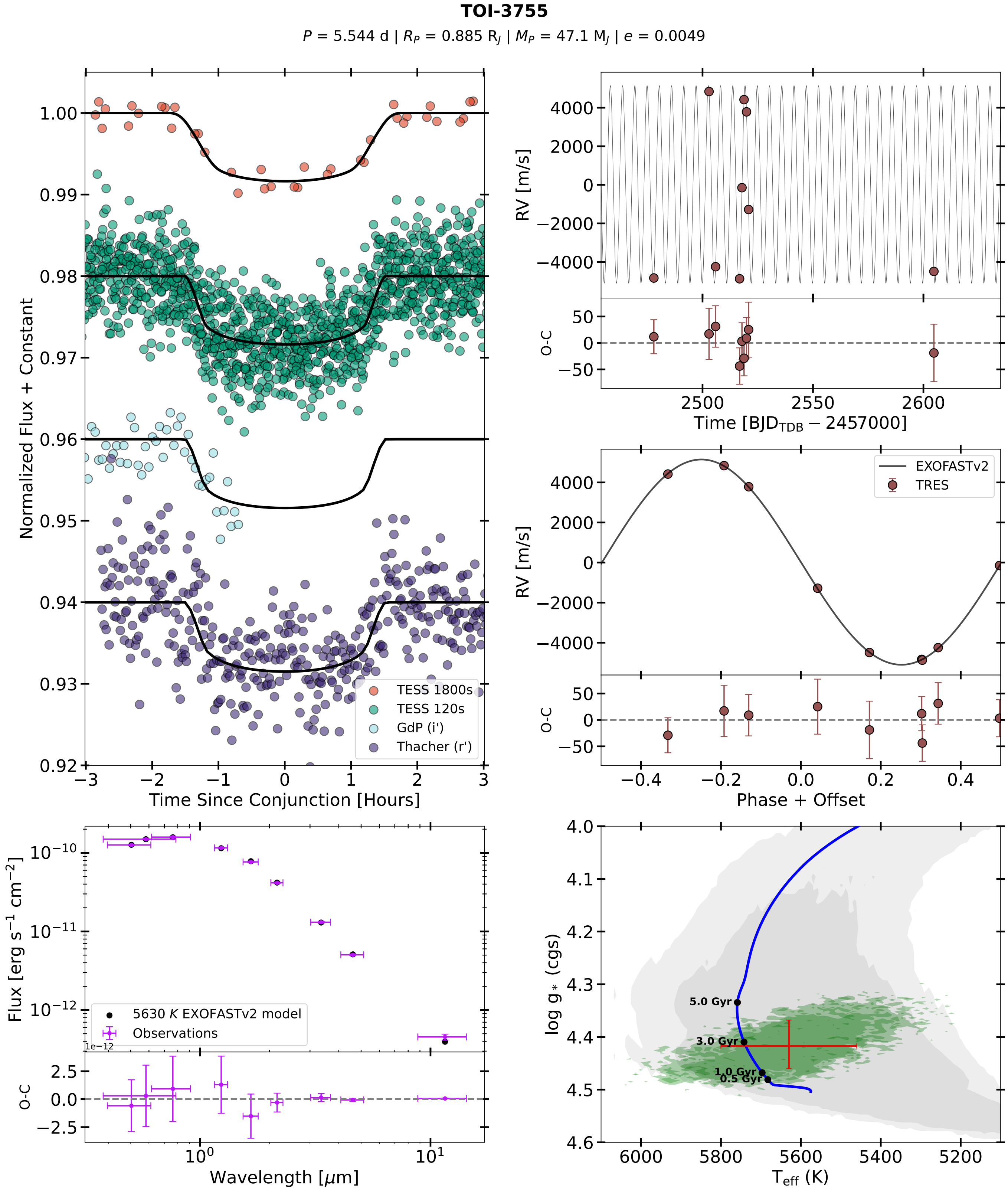

Figure 5. Same as Figure 2 except for TOI-3755.

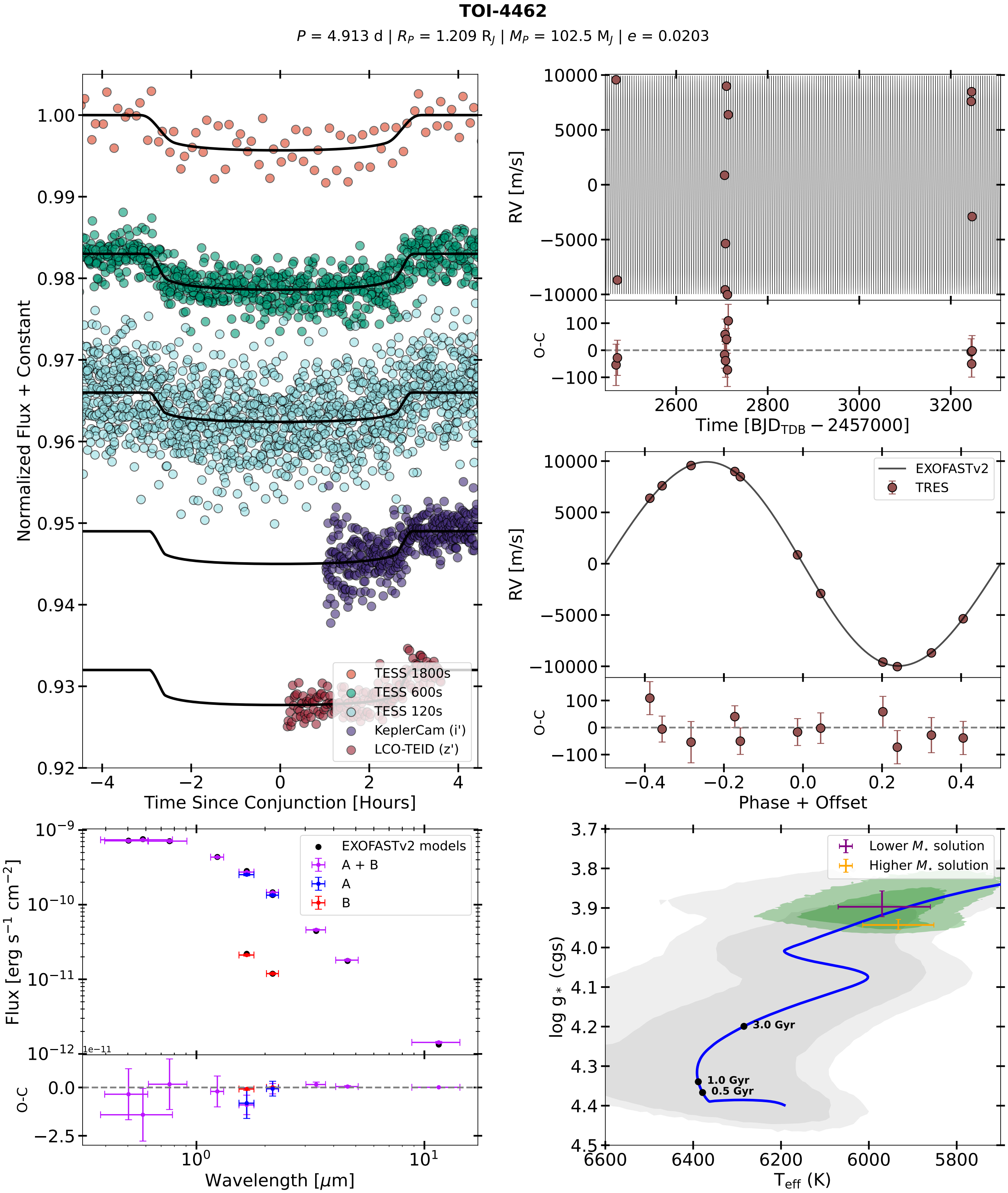

Figure 6. Same as Figure 4 except for TOI-4462. Both TOI-4462 A and B are shown in the bottom left. The `EXOFASTv2` models for TOI-4462 A and B are 5970 K and 4660 K, respectively.

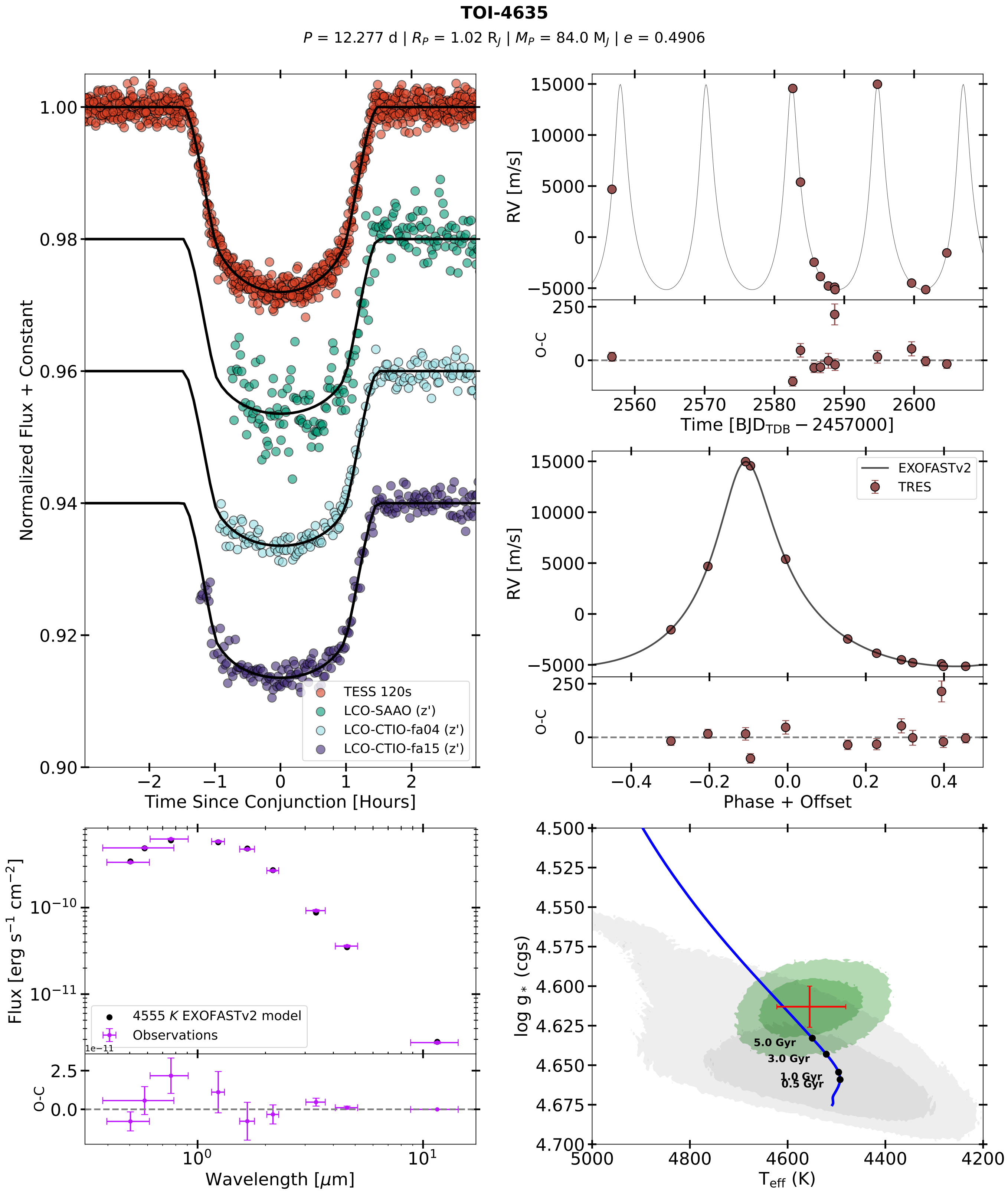

Figure 7. Same as Figure 2 except for TOI-4635.

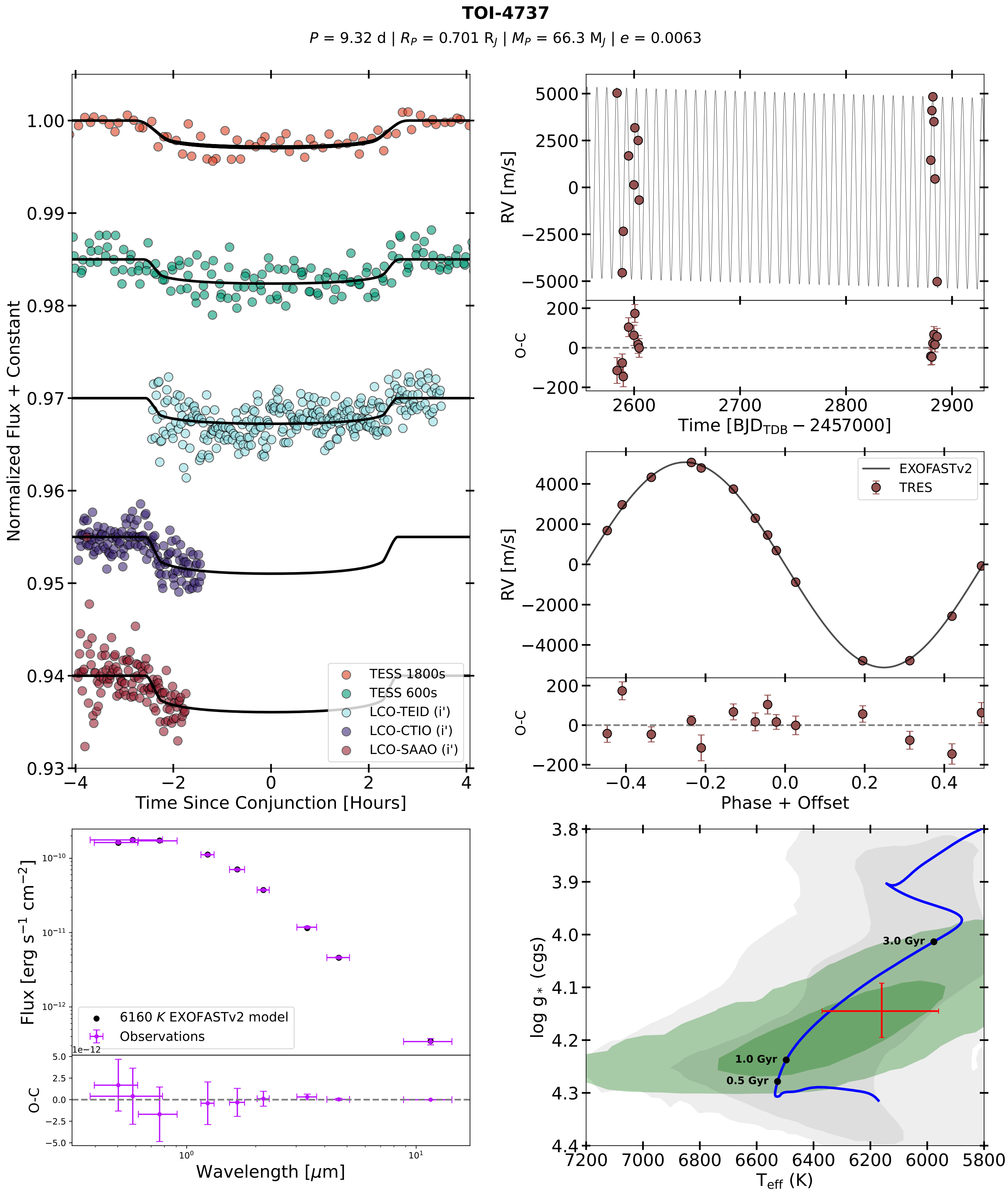

Figure 8. Same as Figure 2 except for TOI-4737.

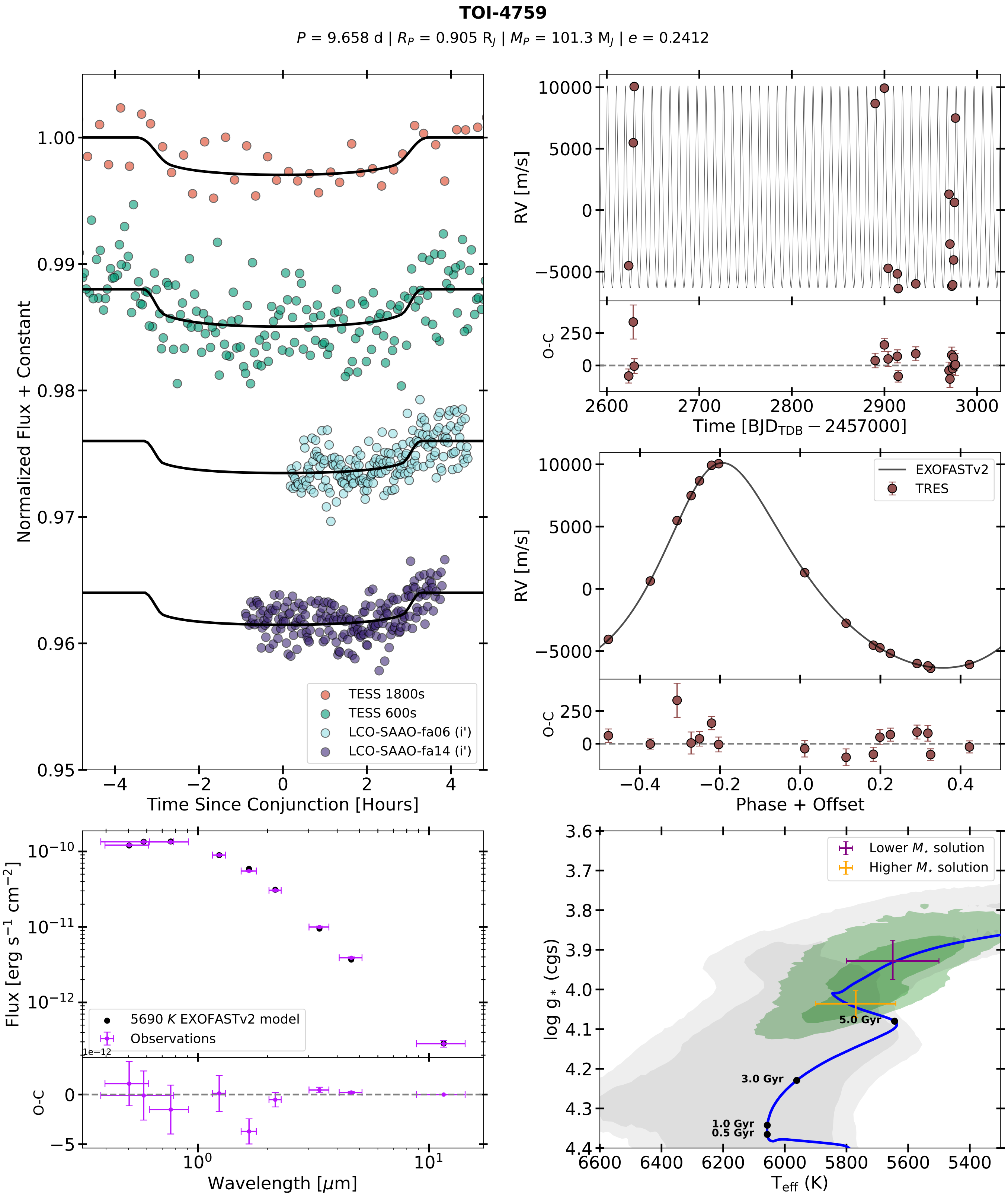

Figure 9. Same as Figure 4 except for TOI-4759.

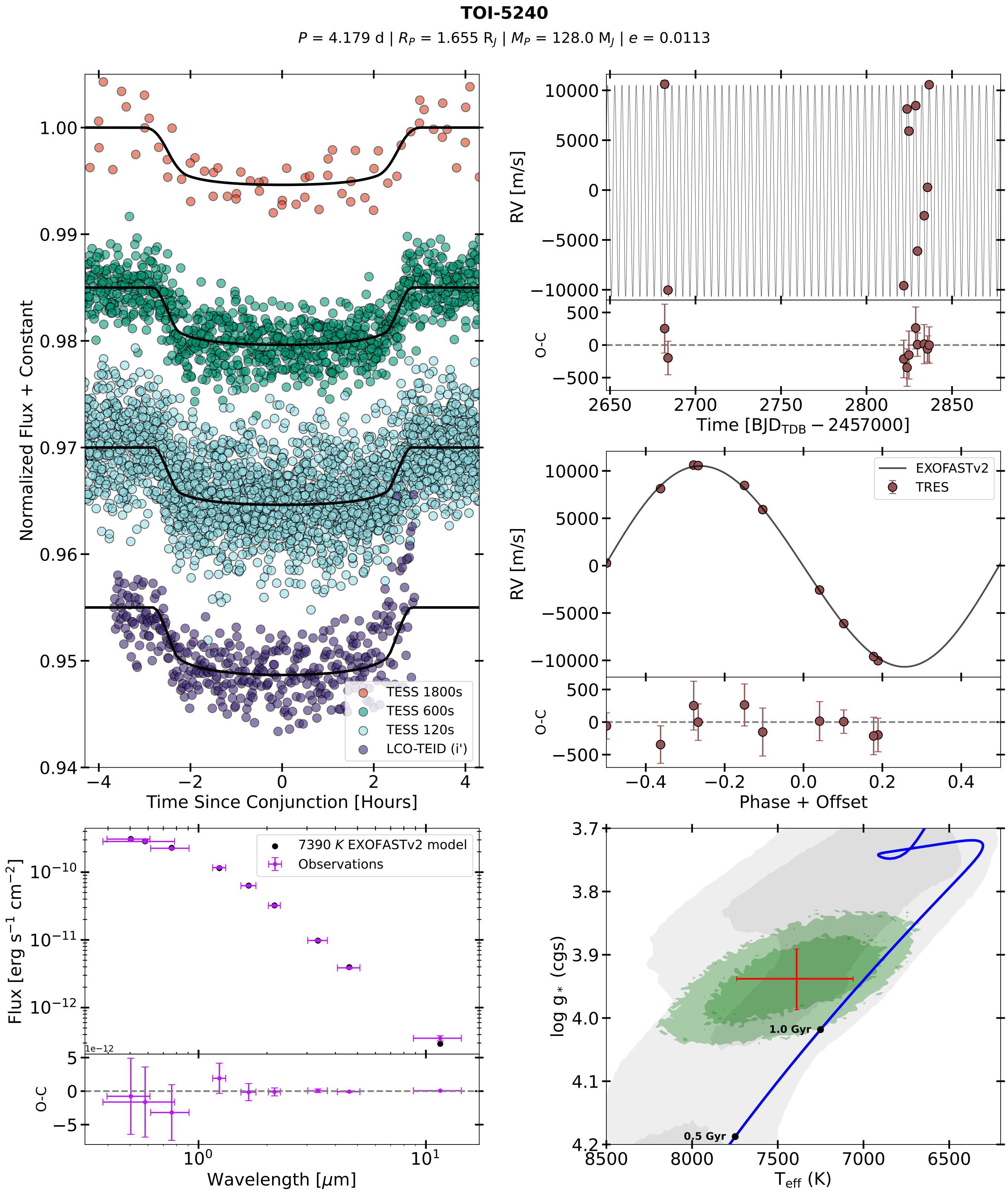

Figure 10. Same as Figure 2 except for TOI-5240.

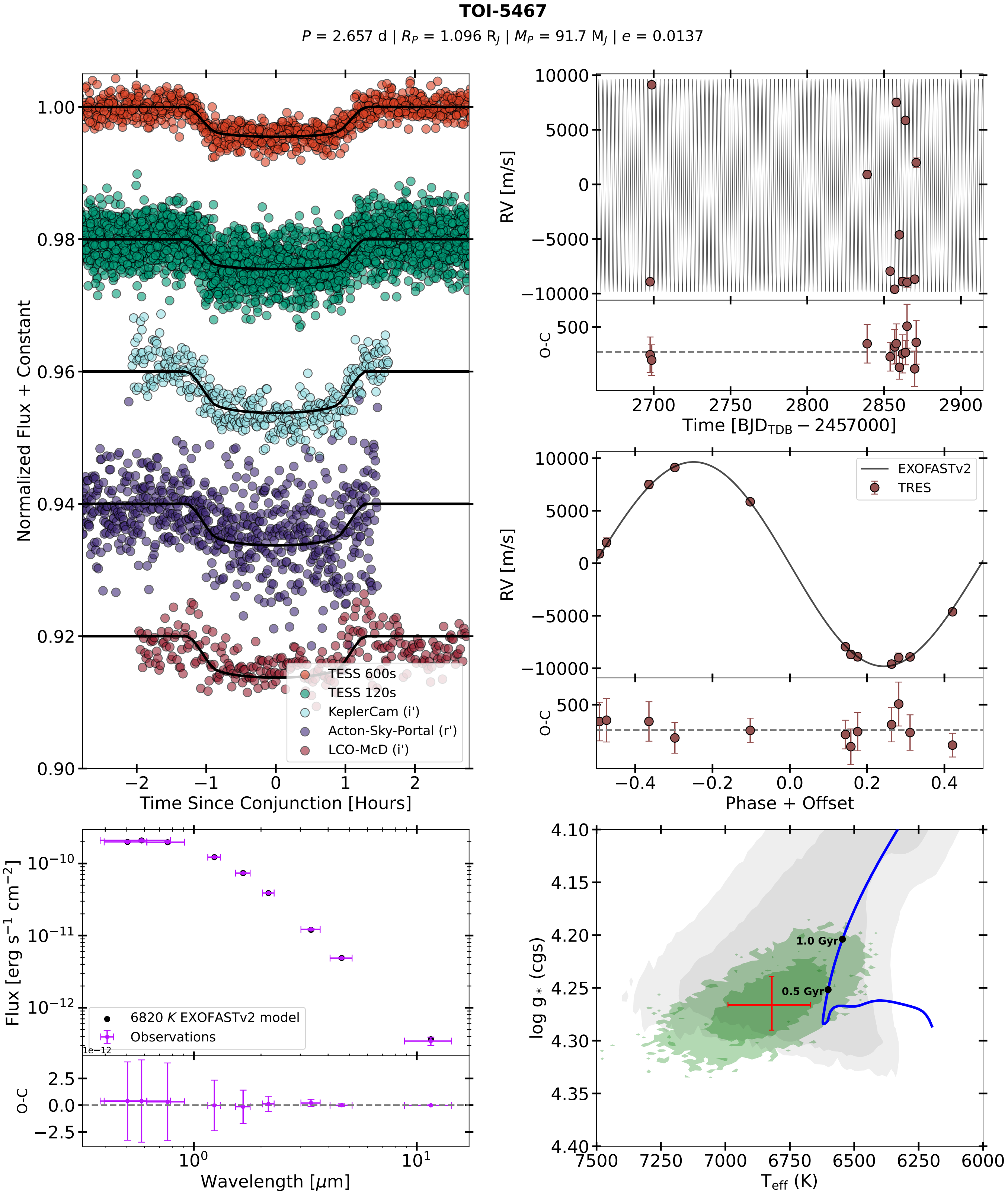

Figure 11. Same as Figure 2 except for TOI-5467.

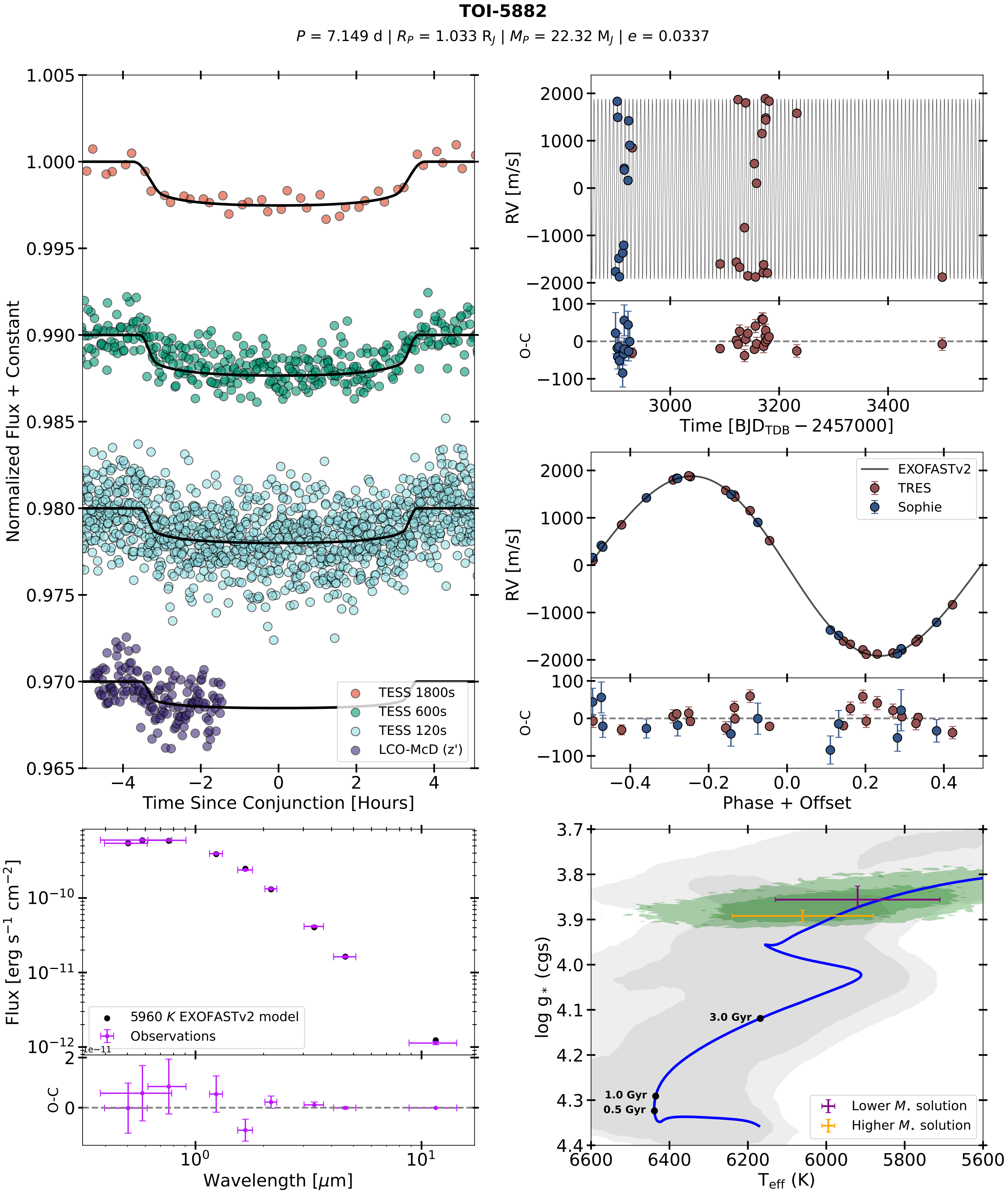

Figure 12. Same as Figure 4 except for TOI-5882.

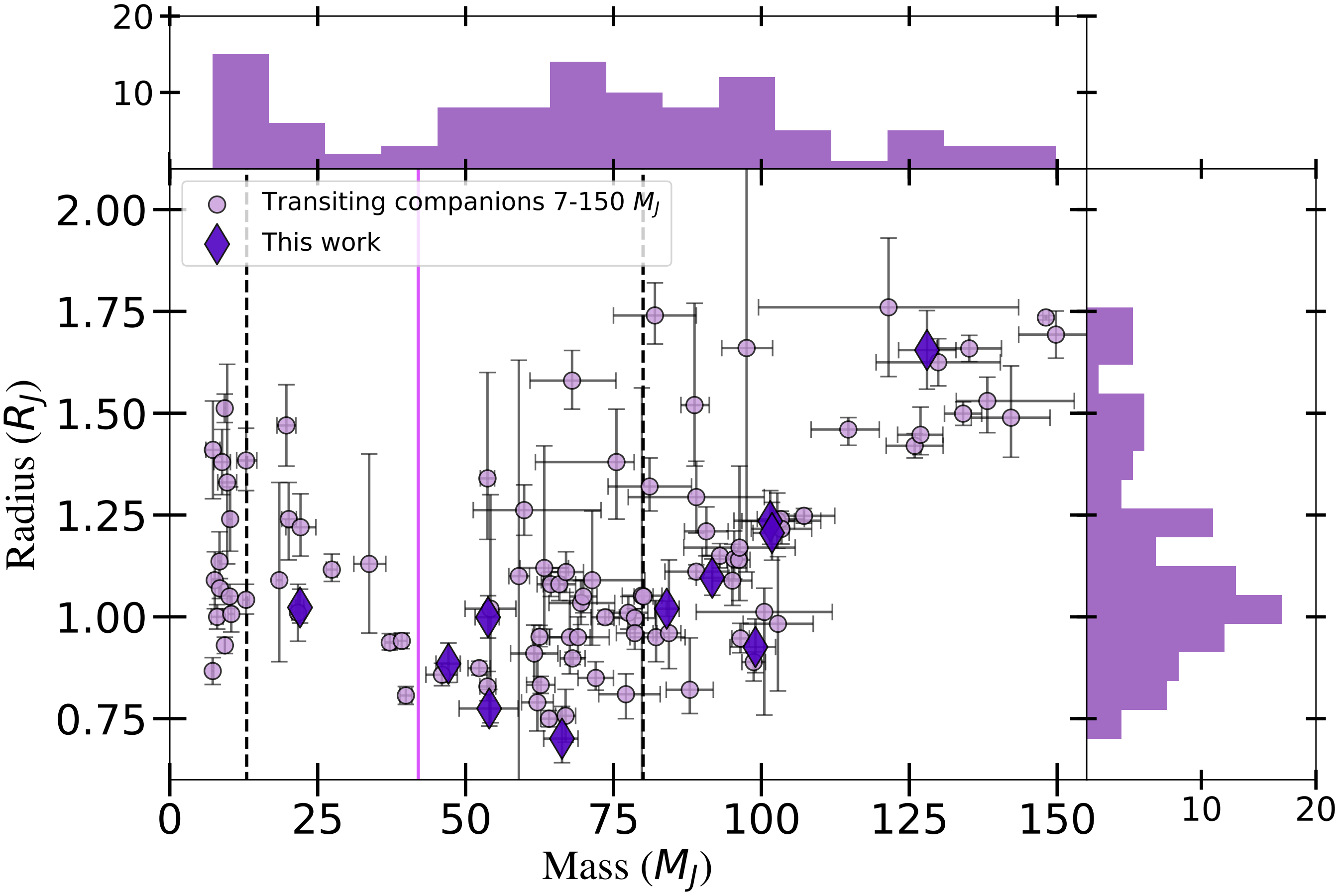

Figure 13. Radius vs. mass for all transiting companions from 7 to 150 M_J. The black dashed lines depict the canonical 13 and 80 M_J BD boundaries. The solid purple line at 42 M_J shows the proposed B. Ma & J. Ge (2014) boundary between planet- and star-like BDs. Note, systems where the primary object is a white dwarf or brown dwarf are not shown. References: B. A. Henderson et al. (2024b) and references therein as well as G. Á. Bakos et al. (2010), L. Buchhave et al. (2011), B. Tingley et al. (2011), H. Parviainen et al. (2014), A. S. Bonomo et al. (2015), L. J. Esteves et al. (2015), K. G. Stassun et al. (2017), J. Bento et al. (2018), C. I. Cañas et al. (2018), B. F. Cooke et al. (2020), P. Cortés-Zuleta et al. (2020), K. El-Badry et al. (2023), M. Lambert et al. (2023), S. P. Schmidt et al. (2023), P. A. Dalba et al. (2024), Y. T. Davis et al. (2024), J. Eberhardt et al. (2023), B. A. Henderson et al. (2024a), M. I. Swayne et al. (2024), and J.-Q. Wang et al. (2024).

their higher-mass counterparts. However, we argue that this trend alone is not necessarily supportive of a 42 M_J transition between the planet and stellar formation mechanisms. If the low-mass transiting BDs are indeed dominated by the planet formation mechanism, then they should be subject to the same evolutionary pathways as the hot Jupiters. The hot Jupiter eccentricity distribution has been shown to be most consistent with high-eccentricity migration mechanisms, and thus are ultimately sculpted by tidal recircularization (J. E. Rodriguez et al. 2023; J. Schulte et al. 2024). We know that this process depends more fundamentally on the mass ratio of the system rather than just the companion mass as evidenced by the tidal recircularization timescale (Equation (2) of F. C. Adams & G. Laughlin 2006). So, if the trend in eccentricity versus companion mass were indeed indicative of a separation between planet-like and star-like formation processes, then we should expect to see the same trends emerge in eccentricity versus mass ratio. Namely, low-mass-ratio systems should exhibit a much smaller range of eccentricities than their high-mass-ratio counterparts. However, as shown in Figure 14 (right), we see the opposite. The eccentricity dichotomy between low- and high-mass companions seems to disappear when plotted against mass ratio. We therefore argue that the eccentricity versus companion mass distribution of transiting companions does not support a 42 M_J transition point.

4.2. Transiting Brown Dwarf Metallicities

Eccentricity is likely not the only parameter that could offer insight into at which critical companion mass the dominant formation mechanism turns over from planet-like to star-like. For nearly three decades we have known of the giant planet–metallicity correlation, in which hot-Jupiter-hosting stars tend to be more metal-rich than their counterparts with no discovered planets (G. Gonzalez 1997; N. C. Santos et al. 2003; D. A. Fischer & J. Valenti 2005). If the low-mass transiting BDs are predominantly forming in the same way as the hot Jupiters, then we should expect their host stars to exhibit the same metallicity enhancement when compared to the high-mass BD hosts. K. C. Schlaufman (2018) tested this hypothesis using the metallicities of transiting companions in the range 0.1–300 M_J to show that transition between core accretion and fragmentation may be as low as 4–10 M_J. However, at the time of this study there were only 27 transiting companions known between 13 and 300 M_J, limiting the ability to probe potential higher-mass transition points. Now that we have access to significantly more systems in this mass regime, we can better probe the same ~42 M_J transition. In Figure 15, we show a preliminary look at testing this hypothesis. Qualitatively, it appears that the lower-mass companions (7–42 M_J) preferentially orbit more metal-rich host stars. However, a two-sample Kolmogorov–Smirnov test yields a

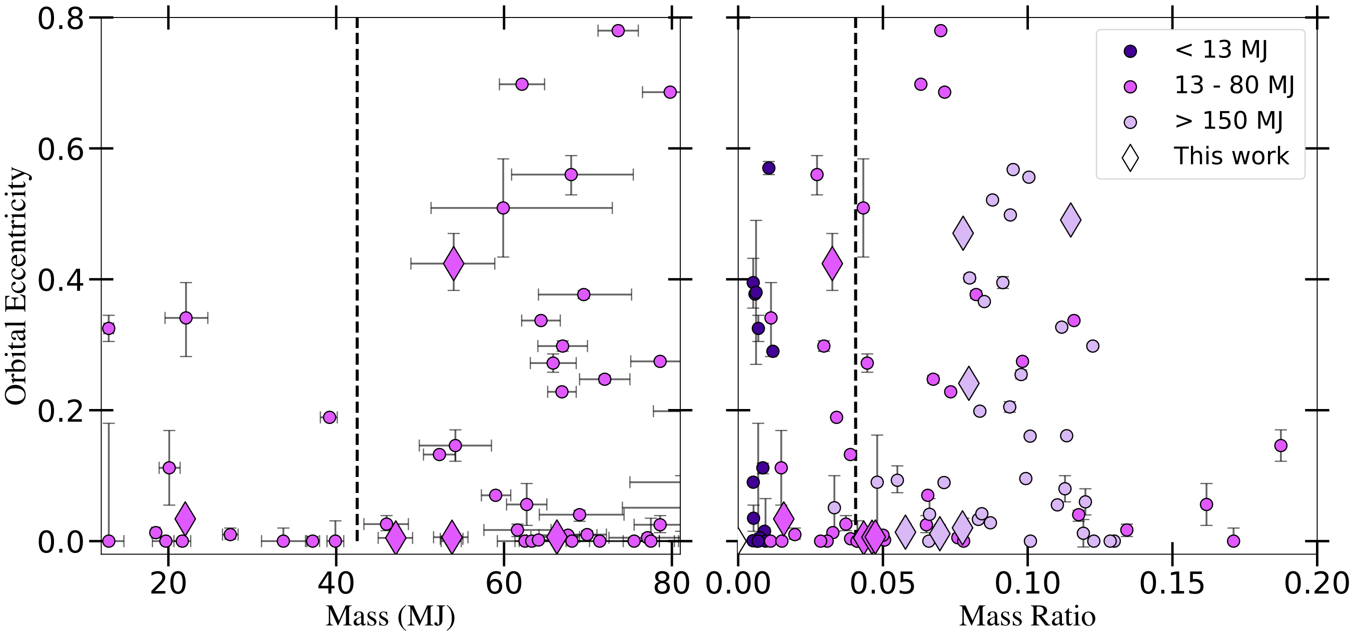

Figure 14. Left: eccentricity vs. mass for transiting BDs with a dotted line at the proposed B. Ma & J. Ge (2014) boundary between planet- and star-like BDs. Right: all transiting companions ranging from 7 to 150 M_J in eccentricity vs. mass ratio with a dashed line at the same 42 M_J location assuming a 1.0 $M_\odot$ host star. As discussed in Section 4.1, the eccentricity dichotomy between low- and high-mass BDs does not hold up when plotted against mass ratio, suggesting that this feature may not represent the boundary between planet-like and star-like BDs.

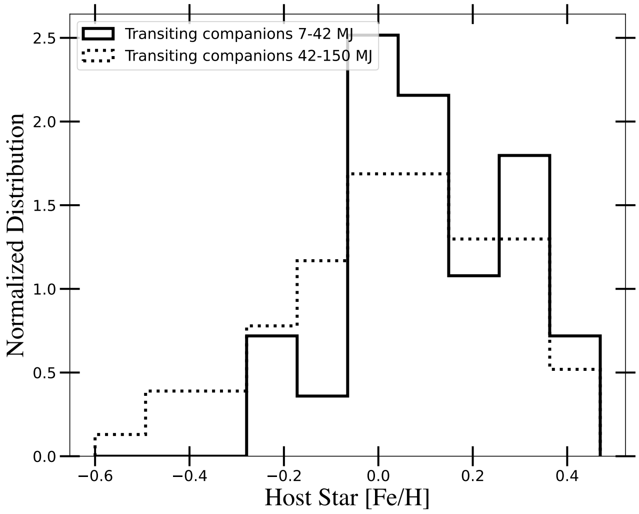

Figure 15. The solid-lined histogram depicts the metallicity distribution of transiting companions ranging from 7 to 42 M_J, while the dotted-lined histogram depicts the metallicity distribution of transiting companions from 42 to 150 M_J. Both histograms are normalized such that their areas are equal to 1. There appears to be a slight trend toward higher metallicities for host stars with lower-mass companions. Note, the metallicities shown here are the values cited by their original discovery papers, and hence represent a heterogeneous sample with a variety of different measurement techniques.

p-value of 0.35, too high to reject the null hypothesis that the high-mass and low-mass samples are drawn from the same underlying distribution.

We note also a few important caveats for interpreting the metallicity distribution. First, we chose a 42 M_J cutoff for historical reasons in order to compare to the original hypothesis presented by B. Ma & J. Ge (2014) as well as the eccentricity distribution presented in Section 4.1. It may be that a more appropriate boundary separating the population will be found after a more comprehensive analysis which may be in better agreement with the lower-mass K. C. Schlaufman (2018) transition. With just 26 companions below 42 M_J in our 7–150 M_J sample, we chose not to investigate possible lower-mass transitions. A more in-depth analysis including the population of giant planets will need to be done to more precisely probe a lower-mass transition. An unbiased sample of the population of companions across the substellar limit will also be required to better understand the selection effects currently affecting this population. We note also that the metallicities presented here are the reported values from each system's discovery, which have been measured using a variety of different techniques, and therefore the underlying biases affecting each measurement are not explored here.

4.3. Lithium Detected in TOI-5882

During our analysis of TOI-5882's spectra, we found a significant absorption feature at 6708 Å, which we attribute to the Li doublet. We measured the equivalent width of this feature using the `specutils` (N. Earl et al. 2022) package in Python (see Figure 16). To perform this measurement, we first coadded all of the observed TRES spectra, after correcting each for the RV shift, to increase the S/N of the Li feature. The resulting coadded echelle order containing Li has an S/N of 56.8. Then, we defined a 1.4 Å region centered on the rest wavelength of the Li doublet at 6707.844 Å to measure the equivalent width. The resulting equivalent width is 71.2 ± 6.89 mÅ, where the uncertainty was estimated using Equation (6) in R. Cayrel (1988).

The presence of Li in stars is typically interpreted as an indicator of youth. This is due to the temperatures and

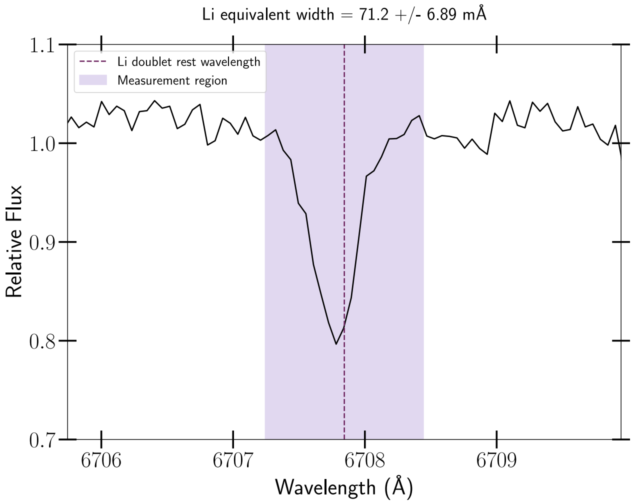

Figure 16. The coadded spectra of TOI-5882 zoomed in to the Li absorption line at 6708 Å. The measurement region used to determine the equivalent width is shaded in purple, with the dashed line at the center indicating the rest wavelength of the Li doublet, 6707.844 Å.

pressures in the core being sufficiently high to destroy Li, which results in Li being visible on the stellar surface slowly depleting as transport occurs between the core and the surface of the star (D. R. Soderblom et al. 2014). Despite this, we claim that TOI-5882 is likely not a young star, since we found no other signs of youth. To verify this, we performed a period search on each sector of TOI-5882's TESS light curves to characterize the rotation of the host star. Since young stars are typically born rapidly rotating and gradually spin down over time, an age can often be inferred from a star's rotation period if it is below the Kraft break (L. G. Bouma et al. 2023). We found a significant peak in the periodogram at 9.6 days; however, we are hesitant to adopt this as the true rotation period since periodicity beyond one-third of a TESS observing sector (∼9 days) can be unreliable due to aliases induced by the TESS observing strategy and processing of light curves. Even if we were to believe that the 9.6 days periodicity is truly due to stellar rotation, it is still anomalous when compared to the observed rotation periods of young stars. T Tauri stars, for example, rarely exhibit rotation periods longer than 8 days (J. Serna et al. 2021), and gyrochronology shows that a 9.6 days period would be indicative of an age of approximately 1 Gyr given this star's effective temperature (L. G. Bouma et al. 2023). While a young age for TOI-5882 cannot be conclusively ruled out by its rotation, it is unlikely, especially combined with the lack of other youth indicators.

For example, we also searched for nearby comoving stars using `FriendFinder` (B. M. Tofflemire et al. 2021),[43] since their presence would indicate that TOI-5882 and its hypothetical nearby comovers have not yet dispersed from their birth location and hence would be young. `FriendFinder` identifies all nearby sources that fall within a selected search radius, and calculates the predicted tangential velocity $v_{\rm tan}$ for each source, assuming that they have Galactic velocity components (U,V,W) identical to TOI-5882. This predicted $v_{\rm tan}$ is then compared to the true $v_{\rm tan}$, which is derived from Gaia proper motions. Using a physical search radius of 30 pc around TOI-5882 and a difference between the predicted and measured $v_{\rm tan}$ of $<5\,{\rm km\,s^{-1}}$, we find no evidence that TOI-5882 is part of a comoving group. Furthermore, the nearest star-forming regions in Cygnus, where TOI-5882 is located, are much further away (>1 kpc; B. Reipurth & N. Schneider 2008).

Finally, we looked for an infrared excess as well as Hα emission. Young stellar objects that retain a circumstellar disk show increased emission at infrared wavelengths (T. H. Cotten & I. Song 2016). We ruled out an infrared excess for TOI-5882 via our SED fitting in the global analysis, where we see no significant infrared emission above the blackbody model in any of the WISE W1, W2, and W3 bandpasses. The presence of Hα lines in emission is also characteristic of active young stars (C. Briceño et al. 2019), and we found no evidence of such emission. While the lack of these additional youth indicators does not completely rule out the possibility of a young host star, we believe it is more likely that TOI-5882 is a late subgiant star, as indicated by our most probable `EXOFASTv2` solution. This older age could then imply that the presence of Li is due to the infall of planetary material onto the host star. For a deeper dive into the origin of Li in TOI-5882, including its potential as a system that has undergone a planetary engulfment, we alert the reader to B. Kotten et al. (2025, in preparation).

5. Conclusions

In this paper, we present the discovery of 11 new transiting companions from the TESS mission. We collected photometric time-series, spectroscopic, and high-resolution imaging follow-up as a part of the TFOP to rule our false positives and further characterize each system. Using `EXOFASTv2`, we performed a global fit on each system using the space- and ground-based transits, spectroscopic RVs, and archival photometry to characterize both the host stars and their transiting companions. We found that five of these systems are brown dwarfs ($13 < M_2 < 80\,M_{\rm J}$) and six of them are very-low-mass stars from $80 < M_2 < 130\,M_{\rm J}$. This contribution to the transiting brown dwarf population increases it to 54 systems, a milestone that represents the population outgrowing the burdens of small sample statistics.

Using this population that TESS has rapidly developed to a significant size, we offered some initial insight into the features that have started to appear. We revisit the idea of the "brown dwarf desert" for the short orbital periods probed by the transit method. We revisited the eccentricity–mass distribution that has been claimed as evidence of a $42\,M_{\rm J}$ transition between planet and star formation, and showed that this trend does not seem to hold in eccentricity versus mass ratio, calling into question whether eccentricity truly does offer insight into the formation mechanisms behind these rare objects. We also examined the metallicity distribution of transiting BD host stars for the first time, and find that a $42\,M_{\rm J}$ transition does not divide the population into two distinct populations with any statistical significance.

Finally, we noted the presence of Li in the spectrum of TOI-5882, the host star of our lowest-mass BD. We measured the equivalent width of the Li line and search for other signs of youth. Seeing no evidence of youth from any of the other indicators that we examined, we adopt the age provided by our global `EXOFASTv2` fit and do not interpret the presence of Li as a sign of youth. Instead, we noted that the Li may actually be a signature of engulfed planetary material, and that more work will be required to explore this hypothesis reported in Table 6.

---

[43] https://github.com/adamkraus/comove

Acknowledgments

This paper includes data collected by the TESS mission that are publicly available from the Mikulski Archive for Space Telescopes (MAST; STScI 2018). Funding for the TESS mission is provided by NASA's Science Mission Directorate. We acknowledge the use of public TESS data from pipelines at the TESS Science Office and at the TESS Science Processing Operations Center. Resources supporting this work were provided by the NASA High-End Computing (HEC) Program through the NASA Advanced Supercomputing (NAS) Division at Ames Research Center for the production of the SPOC data products. This research has made use of the NASA Exoplanet Archive and the Exoplanet Follow-up Observation Program (ExoFOP; DOI: 10.26134/ExoFOP5) website, which is operated by the California Institute of Technology, under contract with the National Aeronautics and Space Administration under the Exoplanet Exploration Program. We acknowledge financial support from the Agencia Estatal de Investigación of the Ministerio de Ciencia e Innovación MCIN/AEI/10.13039/501100011033 and the ERDF "A way of making Europe" through project PID2021-125627OB-C32, and from the Centre of Excellence "Severo Ochoa" award to the Instituto de Astrofisica de Canarias. This work makes use of observations from the LCOGT network. Part of the LCOGT telescope time was granted by NOIRLab through the Mid-Scale Innovations Program (MSIP). MSIP is funded by NSF. This paper is based on observations made with the Las Cumbres Observatory's education network telescopes that were upgraded through generous support from the Gordon and Betty Moore Foundation. Based on observations obtained at the Hale Telescope, Palomar Observatory, as part of a collaborative agreement between the Caltech Optical Observatories and the Jet Propulsion Laboratory operated by Caltech for NASA. D.R.C. and C.A.C. acknowledge partial support from NASA grant 18-2XRP18_2-0007. Based in part on observations obtained at the Southern Astrophysical Research (SOAR) telescope, which is a joint project of the Ministério da Ciência, Tecnologia e Inovações (MCTI/LNA) do Brasil, the U.S. National Science Foundation NOIRLab, the University of North Carolina at Chapel Hill (UNC), and Michigan State University (MSU). This work is partly supported by JSPS KAKENHI grant No. JP24H00017, JP24K00689 and JSPS Bilateral Program Number JPJSBP120249910. This paper is based on observations made with the MuSCAT2 instrument, developed by ABC, at Telescopio Carlos Sánchez operated on the island of Tenerife by the IAC in the Spanish Observatorio del Teide. We thank the staff of the Observatoire de Haute-Provence for their support at the 1.93 m telescope and on SOPHIE.

N.V. is supported by the NASA FINESST program. The postdoctoral fellowship of K.B. is funded by F.R.S.-FNRS grant T.0109.20 and by the Francqui Foundation. K.A.C. and C.N.W. acknowledge support from the TESS mission via subaward s3449 from MIT. I.A.S. acknowledges the support of M.V. Lomonosov Moscow State University Program of Development. F.M. acknowledge support from the Agencia Estatal de Investigación del Ministerio de Ciencia, Innovación y Universidades (MCIU/AEI) through grant PID2023-152906NA-I00. L.M. acknowledges financial contribution from PRIN MUR 2022 project 2022J4H55R. T.F.'s work is supported by the French National Research Agency in the framework of the Investissements d'Avenir program (ANR-15-IDEX-02), through the funding of the "Origin of Life" project of the Grenoble-Alpes University.

ORCID iDs

Noah Vowell https://orcid.org/0000-0002-0701-4005
Joseph E. Rodriguez https://orcid.org/0000-0001-8812-0565
David W. Latham https://orcid.org/0000-0001-9911-7388
Samuel N. Quinn https://orcid.org/0000-0002-8964-8377
Jack Schulte https://orcid.org/0000-0002-7382-0160
Jason D. Eastman https://orcid.org/0000-0003-3773-5142
Allyson Bieryla https://orcid.org/0000-0001-6637-5401
Khalid Barkaoui https://orcid.org/0000-0003-1464-9276
David R. Ciardi https://orcid.org/0000-0002-5741-3047
Karen A. Collins https://orcid.org/0000-0001-6588-9574
Eric Girardin https://orcid.org/0000-0002-5443-3640
Elisabeth Heldridge https://orcid.org/0009-0001-2900-7834
Marziye Jafariyazani https://orcid.org/0000-0001-8019-6661
Brooke Kotten https://orcid.org/0009-0008-5864-9415
Luigi Mancini https://orcid.org/0000-0002-9428-8732
Felipe Murgas https://orcid.org/0000-0001-9087-1245
Norio Narita https://orcid.org/0000-0001-8511-2981
D. J. Radford https://orcid.org/0000-0002-3940-2360
Howard M. Relles https://orcid.org/0009-0009-5132-9520
Avi Shporer https://orcid.org/0000-0002-1836-3120
Melinda Soares-Furtado https://orcid.org/0000-0001-7493-7419
Ivan A. Strakhov https://orcid.org/0000-0003-0647-6133
Carl Ziegler https://orcid.org/0000-0002-0619-7639
César Briceño https://orcid.org/0000-0001-7124-4094
Michael L. Calkins https://orcid.org/0000-0002-2830-5661
Catherine A. Clark https://orcid.org/0000-0002-2361-5812
Kevin I. Collins https://orcid.org/0000-0003-2781-3207
Gilbert A. Esquerdo https://orcid.org/0000-0002-9789-5474
Sergio B. Fajardo-Acosta https://orcid.org/0000-0001-9309-0102
Cristilyn N. Watkins https://orcid.org/0000-0001-8621-6731
Ruixuan He https://orcid.org/0000-0002-5031-7853
Keith Horne https://orcid.org/0000-0003-1728-0304
Jon M. Jenkins https://orcid.org/0000-0002-4715-9460
Andrew W. Mann https://orcid.org/0000-0003-3654-1602
Luca Naponiello https://orcid.org/0000-0001-9390-0988
Enric Palle https://orcid.org/0000-0003-0987-1593
Richard P. Schwarz https://orcid.org/0000-0001-8227-1020
S. Seager https://orcid.org/0000-0002-6892-6948
John Southworth https://orcid.org/0000-0002-3807-3198
Jonathan J. Swift https://orcid.org/0000-0002-9486-818X
Joshua N. Winn https://orcid.org/0000-0002-4265-047X

References

Adams, F. C., & Laughlin, G. 2006, ApJ, 649, 1004
Adams, F. C., Ruden, S. P., & Shu, F. H. 1989, ApJ, 347, 959
Bakos, G. Á., Torres, G., Pál, A., et al. 2010, ApJ, 710, 1724
Baraffe, I., Chabrier, G., Barman, T. S., Allard, F., & Hauschildt, P. H. 2003, A&A, 402, 701
Baranne, A., Queloz, D., Mayor, M., et al. 1996, A&AS, 119, 373
Bate, M. R. 2012, MNRAS, 419, 3115
Bento, J., Hartman, J. D., Bakos, G. Á., et al. 2018, MNRAS, 477, 3406
Bonomo, A. S., Sozzetti, A., Santerne, A., et al. 2015, A&A, 575, A85
Bouchy, F., Díaz, R. F., Hébrard, G., et al. 2013, A&A, 549, A49
Bouchy, F., Hebrard, G., Udry, S., Delfosse, X., Boisse, I., et al. 2009, A&A, 505, 853
Bouma, L. G., Palumbo, E. K., & Hillenbrand, L. A. 2023, ApJL, 947, L3
Briceño, C., Calvet, N., Hernández, J., et al. 2019, AJ, 157, 85
Brown, T. M., Baliber, N., Bianco, F. B., et al. 2013, PASP, 125, 1031
Buchhave, L. A., Bakos, G. Á., Hartman, J. D., et al. 2010, ApJ, 720, 1118
Buchhave, L. A., Latham, D. W., Carter, J. A., et al. 2011, ApJS, 197, 3

Buchhave, L. A., Latham, D. W., Johansen, A., et al. 2012, Natur, 486, 375
Burrows, A., Hubbard, W. B., Lunine, J. I., & Liebert, J. 2001, RvMP, 73, 719
Burrows, A. S. 2014, Natur, 513, 345
Cañas, C. I., Bender, C. F., Mahadevan, S., et al. 2018, ApJL, 861, L4
Caldwell, D. A., Tenenbaum, P., Twicken, J. D., et al. 2020, RNAAS, 4, 201
Carmichael, T. W., Quinn, S. N., Mustill, A. J., et al. 2020, AJ, 160, 53
Carmichael, T. W., Quinn, S. N., Zhou, G., et al. 2021, AJ, 161, 97
Cayrel, R. 1988, in IAU Symp. 132, The Impact of Very High S/N Spectroscopy on Stellar Physics, ed. G. Cayrel de Strobel & M. Spite (Cambridge: Cambridge Univ. Press), 345
Chabrier, G., Johansen, A., Janson, M., & Rafikov, R. 2014, in Protostars and Planets VI, ed. H. Beuther, R. S. Klessen, C. P. Dullemond, & T. Henning (Tucson, AZ: Univ. Arizona Press), 619
Collins, K. A., Collins, K. I., Pepper, J., et al. 2018, AJ, 156, 234
Collins, K. A., Kielkopf, J. F., Stassun, K. G., & Hessman, F. V. 2017, AJ, 153, 77
Cooke, B. F., Pollacco, D., Almleaky, Y., et al. 2020, AJ, 159, 255
Cortés-Zuleta, P., Rojo, P., Wang, S., et al. 2020, A&A, 636, A98
Cotten, T. H., & Song, I. 2016, ApJS, 225, 15
Cutri, R. M., Skrutskie, M. F., van Dyk, S., et al. 2003, yCat, 2246, 0
Cutri, R. M., Wright, E. L., T., C., et al. 2012, yCat, 2311, 0
Dalba, P. A., Kane, S. R., Isaacson, H., et al. 2024, ApJS, 271, 16
David, T. J., Hillenbrand, L. A., Gillen, E., et al. 2019, ApJ, 872, 161
Davis, Y. T., Triaud, A. H. M. J., Freckelton, A. V., et al. 2024, MNRAS, 530, 2565
Earl, N., Tollerud, E., O'Steen, R., et al. 2022, astropy/specutils: v1.9.1, Zenodo, doi: 10.5281/zenodo.7348235
Eastman, J., Gaudi, B. S., & Agol, E. 2013, PASP, 125, 83
Eastman, J. D., Diamond-Lowe, H., & Tayar, J. 2023, AJ, 166, 132
Eastman, J. D., Rodriguez, J. E., Agol, E., et al. 2019, arXiv:1907.09480
Eberhardt, J., Hobson, M. J., Henning, T., et al. 2023, AJ, 166, 271
El-Badry, K., Burdge, K. B., van Roestel, J., & Rodriguez, A. C. 2023, OJAp, 6, 33
Esteves, L. J., De Mooij, E. J. W., & Jayawardhana, R. 2015, ApJ, 804, 150
Fischer, D. A., & Valenti, J. 2005, ApJ, 622, 1102
Gaia Collaboration, Vallenari, A., Brown, A. G. A., et al. 2023, A&A, 674, A1
Gavel, D., Kupke, R., Dillon, D., et al. 2014, Proc. SPIE, 9148, 914805
Gillen, E., Hillenbrand, L. A., David, T. J., et al. 2017, ApJ, 849, 11
Gonzalez, G. 1997, MNRAS, 285, 403
Grether, D., & Lineweaver, C. H. 2006, ApJ, 640, 1051
Grieves, N., Bouchy, F., Lendl, M., et al. 2021, A&A, 652, A127
Guerrero, N. M., Seager, S., Huang, C. X., et al. 2021, ApJS, 254, 39
Hayward, T. L., Brandl, B., Pirger, B., et al. 2001, PASP, 113, 105
Heidari, N., Boisse, I., Hara, N. C., et al. 2024, A&A, 681, A55
Heidari, N., Hébrard, G., Martioli, E., et al. 2025, A&A, 694, A36
Henderson, B. A., Casewell, S. L., Goad, M. R., et al. 2024a, MNRAS, 530, 318
Henderson, B. A., Casewell, S. L., Jordán, A., et al. 2024b, MNRAS, 533, 2823
Huang, C. X., Vanderburg, A., Pál, A., et al. 2020a, RNAAS, 4, 204
Huang, C. X., Vanderburg, A., Pál, A., et al. 2020b, RNAAS, 4, 206
Jenkins, J. M., Twicken, J. D., McCauliff, S., et al. 2016, Proc. SPIE, 9913, 99133E
Kratter, K., & Lodato, G. 2016, ARA&A, 54, 271
Kunimoto, M., Daylan, T., Guerrero, N., et al. 2022, ApJS, 259, 33
Kunimoto, M., Huang, C., Tey, E., et al. 2021, RNAAS, 5, 234
Kupke, R., Gavel, D., Roskosi, C., et al. 2012, Proc. SPIE, 8447, 84473G
Lambert, M., Bender, C. F., Kanodia, S., et al. 2023, AJ, 165, 218
Latham, D. W., Stefanik, R. P., Mazeh, T., Torres, G., & Carney, B. W. 1998, in ASP Conf. Ser. 134, Brown Dwarfs and Extrasolar Planets, ed. R. Rebolo, E. L. Martin, & M. R. Zapatero Osorio (San Francisco, CA: ASP), 178
Lightkurve Collaboration, Cardoso, J. V. d. M., Hedges, C., et al. 2018, Lightkurve: Kepler and TESS time series analysis in Python, Astrophysics Source Code Library, ascl:1812.013
Lindegren, L., Bastian, U., Biermann, M., et al. 2021, A&A, 649, A4
Ma, B., & Ge, J. 2014, MNRAS, 439, 2781
Marcy, G. W., Butler, R. P., Williams, E., et al. 1997, ApJ, 481, 926
McGurk, R., Rockosi, C., Gavel, D., et al. 2014, Proc. SPIE, 9148, 91483A
Mugrauer, M., & Michel, K.-U. 2020, AN, 341, 996
Mugrauer, M., & Michel, K.-U. 2021, AN, 342, 840
Narita, N., Fukui, A., Kusakabe, N., et al. 2019, JATIS, 5, 015001
NExScI 2022, Exoplanet Follow-up Observing Program Web Service,
Nowak, G., Palle, E., Gandolfi, D., et al. 2017, AJ, 153, 131
Page, E., Pepper, J., Wright, D., et al. 2024, AJ, 167, 109
Parviainen, H., Gandolfi, D., Deleuil, M., et al. 2014, A&A, 562, A140
Parviainen, H., Tingley, B., Deeg, H. J., et al. 2019, A&A, 630, A89
Paxton, B., Bildsten, L., Dotter, A., et al. 2011, ApJS, 192, 3
Paxton, B., Cantiello, M., Arras, P., et al. 2013, ApJS, 208, 4
Pepe, F., Mayor, M., Galland, F., et al. 2002, A&A, 388, 632
Perruchot, S., Kohler, D., Bouchy, F., et al. 2008, Proc. SPIE, 7014, 70140J
Phillips, M. W., Tremblin, P., Baraffe, I., et al. 2020, A&A, 637, A38
Pollack, J. B., Hubickyj, O., Bodenheimer, P., et al. 1996, Icar, 124, 62
Quinn, S. N., White, R. J., Latham, D. W., et al. 2012, ApJL, 756, L33
Reipurth, B., & Schneider, N. 2008, in Handbook of Star Forming Regions, Volume I: The Northern Sky, ed. B. Reipurth, Vol. 4 (San Francisco, CA: ASP), 36
Ricker, G. R., Winn, J. N., Vanderspek, R., et al. 2015, JATIS, 1, 014003
Rodriguez, J. E., Quinn, S. N., Vanderburg, A., et al. 2023, MNRAS, 521, 2765
Safonov, B. S., Lysenko, P. A., & Dodin, A. V. 2017, AstL, 43, 344
Santos, N. C., Israelian, G., Mayor, M., Rebolo, R., & Udry, S. 2003, A&A, 398, 363
Saumon, D., & Marley, M. S. 2008, ApJ, 689, 1327
Schlafly, E. F., & Finkbeiner, D. P. 2011, ApJ, 737, 103
Schlaufman, K. C. 2018, ApJ, 853, 37
Schlegel, D. J., Finkbeiner, D. P., & Davis, M. 1998, ApJ, 500, 525
Schmidt, S. P., Schlaufman, K. C., Ding, K., et al. 2023, AJ, 166, 225
Schulte, J., Rodriguez, J. E., Bieryla, A., et al. 2024, AJ, 168, 32
Scott, N. J., Howell, S. B., Horch, E. P., & Everett, M. E. 2018, PASP, 130, 054502
Serna, J., Hernandez, J., Kounkel, M., et al. 2021, ApJ, 923, 177
Skrutskie, M. F., Cutri, R. M., Stiening, R., et al. 2006, AJ, 131, 1163
Soderblom, D. R., Hillenbrand, L. A., Jeffries, R. D., Mamajek, E. E., & Naylor, T. 2014, in Protostars and Planets VI, ed. H. Beuther, R. S. Klessen, C. P. Dullemond, T. Henning et al. (Tucson, AZ: Univ. Arizona Press), 219
Spiegel, D. S., Burrows, A., & Milsom, J. A. 2011, ApJ, 727, 57
Stassun, K. G., Collins, K. A., & Gaudi, B. S. 2017, AJ, 153, 136
Stassun, K. G., Oelkers, R. J., Paegert, M., et al. 2019, AJ, 158, 138
Stassun, K. G., Oelkers, R. J., Pepper, J., et al. 2018, AJ, 156, 102
Stevens, D. J., Gaudi, B. S., & Stassun, K. G. 2018, ApJ, 862, 53
Strakhov, I. A., Safonov, B. S., & Cheryasov, D. V. 2023, AstBu, 78, 234
STScI 2018, TESS Input Catalog and Candidate Target List, MAST, doi:10.17909/FWDT-2X66
Šubjak, J., Sharma, R., Carmichael, T. W., et al. 2020, AJ, 159, 151
Swayne, M. I., Maxted, P. F. L., Triaud, A. H. M. J., et al. 2024, MNRAS, 528, 5703
Swift, J. J., Andersen, K., Arculli, T., et al. 2022, PASP, 134, 035005
Tingley, B., Endl, M., Gazzano, J. C., et al. 2011, A&A, 528, A97
Tofflemire, B. M., Rizzuto, A. C., Newton, E. R., et al. 2021, AJ, 161, 171
Tokovinin, A. 2018, PASP, 130, 035002
Twicken, J. D., Catanzarite, J. H., Clarke, B. D., et al. 2018, PASP, 130, 064502
Vanderburg, A., & Johnson, J. A. 2014, PASP, 126, 948
Vowell, N., Rodriguez, J. E., Quinn, S. N., et al. 2023, AJ, 165, 268
Wang, J.-Q., Jiang, X.-J., Zheng, J., et al. 2024, RAA, 24, 035012
Wright, E. L., Eisenhardt, P. R. M., Mainzer, A. K., et al. 2010, AJ, 140, 1868
Ziegler, C., Tokovinin, A., Briceño, C., et al. 2020, AJ, 159, 19